ENCYCLOPEDIA OF VOLCANOES (3RD EDITION)

PART 3: Volcanic eruptions and associated products

Section 4: Explosive eruptions

Chapter 4.3 - Tephra fallout and associated deposits

Marco Pistolesi[1], Paul Albert[2], Alvaro Aravena[3], Samantha Engwell[4], Ulrich Kueppers[5], Federica Pardini[6], Kae Tsunematsu[7], Alexa R. Van Eaton[8]

[1]University of Pisa, Italy
[2]Swansea University, UK
[3]Universidad Católica del Maule, Chile
[4]British Geological Survey, UK
[5]Ludwig-Maximilians-Universität (LMU) Munich, Germany
[6]Istituto Nazionale di Geofisica e Vulcanologia, Italy
[7]Yamagata University, Japan
[8]U.S. Geological Survey, Cascades Volcano Observatory, Vancouver, Washington, USA

This is a peer-reviewed preprint submitted to *EarthArXiv*. The manuscript is part of Chapter 4.3 of forthcoming book: The Encyclopedia of Volcanoes, 3rd ed. Editors: C. Bonadonna, L. Caricchi, A. Clarke, P. Cole, J. Lindsay, J. Lowenstern, R. Robertson and M.L. Villegas, that will be published by Elsevier. As one of the first 20 chapters to be accepted for publication in the book, it is being allowed to be submitted to *EarthArXiv* as a preprint.

ENCYCLOPEDIA OF VOLCANOES (3RD EDITION)

PART 3: Volcanic eruptions and associated products

Section 4: Explosive eruptions

Chapter 4.3 - Tephra fallout and associated deposits

Marco Pistolesi[1], Paul Albert[2], Alvaro Aravena[3], Samantha Engwell[4], Ulrich Kueppers[5], Federica Pardini[6], Kae Tsunematsu[7], Alexa R. Van Eaton[8]

[1]University of Pisa, Italy
[2]Swansea University, UK
[3]Universidad Católica del Maule, Chile
[4]British Geological Survey, UK
[5]Ludwig-Maximilians-Universität (LMU) Munich, Germany
[6]Istituto Nazionale di Geofisica e Vulcanologia, Italy
[7]Yamagata University, Japan
[8]U.S. Geological Survey, Cascades Volcano Observatory, Vancouver, Washington, USA

Abstract

The lifecycle of volcanic fall deposits begins with explosive fragmentation, continues as particles rise through the atmosphere, and culminates with sedimentation on the ground. This chapter explores how fall deposits can reveal the unique eruption and transport processes that shaped them. While we can directly observe modern eruptions to understand their dynamics, unobserved volcanic events are reconstructed through their deposits. This process typically includes field and laboratory-based measurements of tephra dispersal, grain size, componentry, composition, and clast textures. Advances in modern observational techniques and numerical modeling have also enhanced our understanding of tephra transport and forecasting of the hazards related to airborne ash. Using a combination of these approaches to link field deposits with their sub-visible equivalents in the distal realm (cryptotephra) provide key chrono-stratigraphic markers for records of eruption history on regional to global scales.

Keywords

Tephra – Fallout – Tephrostratigraphy – Ash – Lapilli – Pumice – Scoria – Grain size – Fragmentation

Introduction

The Greek term *tephra* refers to clasts ejected during a volcanic eruption, regardless of size, shape, composition, or emplacement mechanism[1]. These clasts are classified as ash (<2 mm), lapilli (2–64 mm), and blocks or bombs (>64 mm) depending on their size. In this chapter, we focus on tephra-fall deposits, which come to rest after falling through the atmosphere rather than by lateral transport in ground-hugging pyroclastic density currents[E1].

Direct observation of erupting volcanoes has allowed for broad empirical understanding of the processes governing tephra transport and dispersal. However, many eruptions cannot be accessed for close-in observation due to their remote location or extreme hazard. In these cases, tephra deposits can be used to reconstruct the timeline of eruption dynamics, including specific processes such as ballistic ejection, turbulent transport in the volcanic plume[E2], and particle aggregation before fallout. Furthermore, characteristic features of tephra fall deposits as a function of distance from source provide a global framework for classifying eruptions of different style (e.g., Hawaiian, Strombolian, Violent Strombolian, Vulcanian, Subplinian, Plinian, Surtseyan, Phreatoplinian[E3]).

Laboratory and field investigations on proximal deposits are commonly combined to define their overall sedimentological characteristics and complemented by analysis of single (or thousands of) clasts from the corresponding deposits to define textural, physical, and compositional features of juvenile material. A specific branch of studies uses distal (i.e. hundreds to thousands of km from the source), discrete tephra beds or dispersed volcanic fragments in clastic sediments, which can be geochemically fingerprinted and correlated over wide geographical distances, to provide temporal stratigraphic markers (tephrostratigraphy) and thus tools for synchronizing volcanic activity at a regional scale or paleoclimate archives (lacustrine, marine and ice cores). Where tephra fallout layers are correlated to dated eruptive events, they provide absolute age constraints on host records (tephrochronology), and thus distal tephra fallout can contribute to improve reconstructions of past geological events (regional tectonics, paleoceanography, paleoclimatology). Numerical modeling of tephra fallout uses physical simulation of tephra dispersal in the atmosphere and sedimentation on the ground to retrieve eruption source parameters or to forecast tephra concentration in the air, dispersal direction and tephra accumulation during eruption crises.

Magma fragmentation and generation of tephra

The diversity of pyroclast textures is testament to the wide range of processes controlling magma fragmentation as it rises from depth and erupts at the surface. Long-term processes operate over decades to millennia to accumulate magma in a reservoir and evolve its composition. Conversely, rapid changes in the shallow conduit govern magma degassing and fragmentation dynamics and/or interaction with external factors (e.g., contact with external water or conduit collapse) on timescales of minutes or less. Magma ascent cannot be directly observed, but important insights can be deduced from the geochemistry and textures of erupted pyroclasts, numerical modeling of volcanic conduits, and laboratory experiments that connect magma characteristics – such as tensile strength and porosity – with fragmentation behavior[2,3].

The origin of tephra begins with bubble nucleation, as magma rises through the crust and confining pressure decreases (Figure 1). Volatiles initially dissolved in the melt reach supersaturation and begin to exsolve, forming gas bubbles in a process known as degassing. The onset of supersaturation depends on melt composition, confining pressure, temperature, and the bulk volatile content as well as the ratio of different volatile species. Initially, bubbles are small and dispersed within the melt, but they grow during chemical diffusion (as volatile molecules diffuse from the melt to bubbles) and decompression.

These bubbles can coalesce or mechanically separate from the melt, which is known as outgassing. Subsequent volatile loss can trigger microlite crystallization in a run-away effect that leads to more gas exsolution, a process termed second boiling. The abundance of bubbles and crystals strongly influences the rheological behavior of the magma and its ascent dynamics. When critical conditions are reached, local stress accumulation leads to magma fragmentation.

Primary, magmatic fragmentation occurs when a coherent batch of magma disintegrates into smaller particles known as pyroclasts[4]. Fragmentation tends to be dominated by brittle processes, triggered by a combination of high strain rates and gas overpressure that cause magma to fracture. Many of these fractures occur along bubble walls, leading to cuspate shapes preserved in shards of volcanic glass. The presence of external water (Figure 1c) promotes additional breakup due to rapid heat transfer across magma–water interfaces[5], leading to hydrovolcanic (or phreatomagmatic) fragmentation. Even in cases where magma does not directly reach the surface, magmatic heating of groundwater can produce phreatic, steam-driven eruptions that explosively fragment the surrounding rock[E3]. In the case of low-viscosity magmas such as basalt, magma is more likely to undergo ductile (inertia-controlled) deformation during eruption (Figure 1b). This process creates fluidal clasts, like the Pele's hair or tears observed from lava fountains or bubbles bursting at the lava surface.

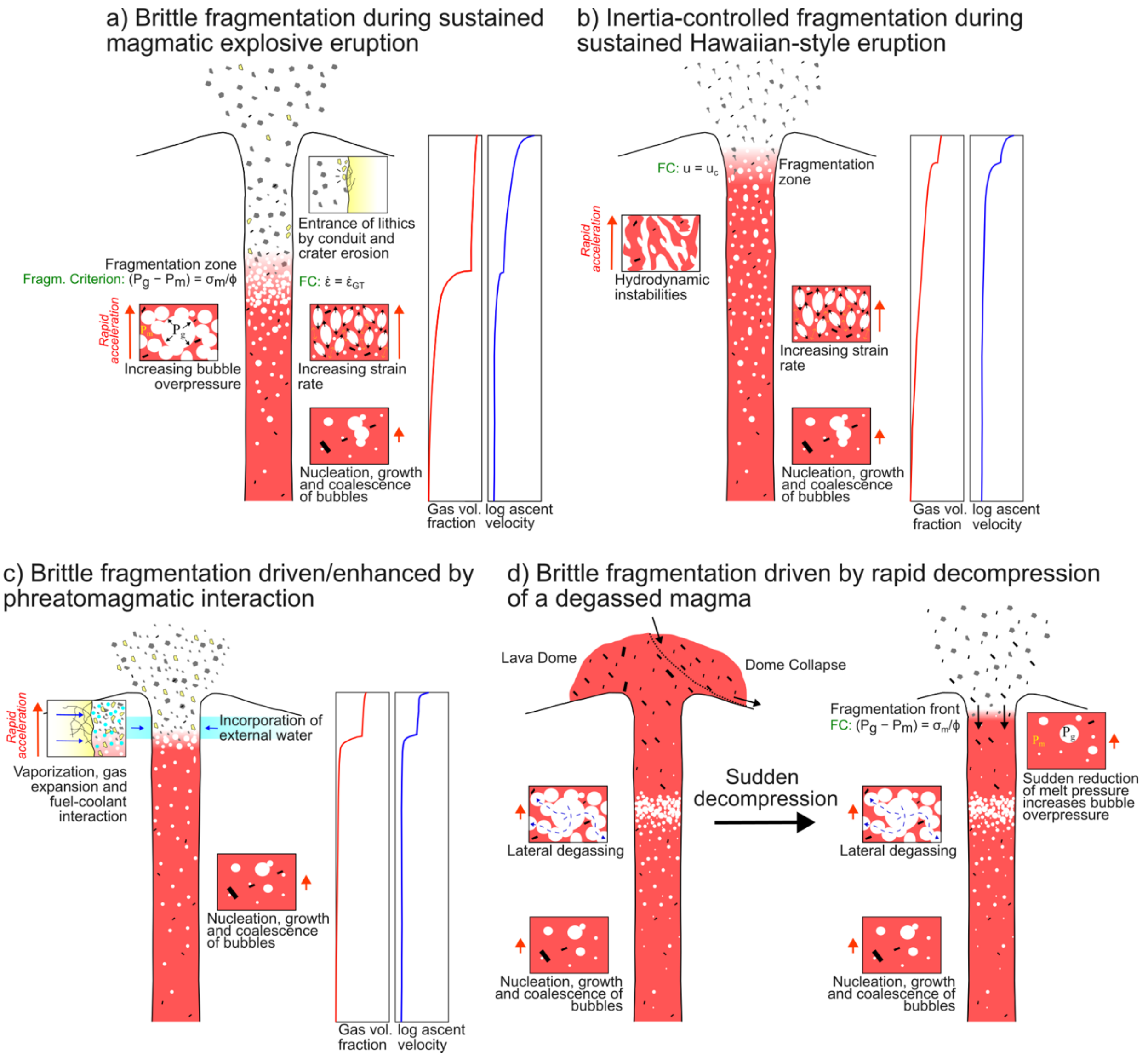

Figure 1. Different fragmentation mechanisms modified from [2]. During the flow of porous magma towards

Earth's surface, bubble overpressure and/or strain rate can increase. (a) In sustained magmatic eruptions, overpressure and strain rate may trigger predominantly brittle fragmentation. (b) If initially low-viscosity magma rises, ductile fragmentation can be a consequence of hydrodynamic instabilities in the uppermost conduit or the lava fountain. (c) Heat transfer from magma to external water under confinement, the resulting sudden volume increase of steam and contemporaneous cooling of magma (fuel-coolant interaction) lead to strongly increased shear conditions locally and may alter significantly the eruptive style. (d) Gravitational unloading of magma in cryptodomes or the conduit may trigger fragmentation due to a sudden increase of bubble overpressure, as occurred during the 18 May 1980 eruption of Mount St. Helens (Case Study box 1). A set of frequently adopted criteria for magma fragmentation is included, where P_g is bubble pressure, P_m is melt pressure, σ_m is the effective tensile strength of magma, ϕ is vesicularity, $\dot{\varepsilon}$ is the magma strain rate, $\dot{\varepsilon}_{GT}$ is the glass transition strain rate, υ is ascent velocity of magma, and υ_c is the critical velocity for inertia-controlled fragmentation.

Upon fragmentation, the explosive release of gas accelerates the erupting mixture into the upper conduit and atmosphere. Excavation and widening of the conduit walls may incorporate fragments of pre-existing rock. At this point, secondary fragmentation takes over in the lower eruption column and in ground-hugging pyroclastic density currents. Energetic collisions and continued degassing of larger clasts lead to additional breakup and production of fine ash in particle-laden flows.

Tephra transport and sedimentation

After eruption into the atmosphere, tephra particles can take many different paths. The gas-particle mixture may rise at velocities much faster than the background wind field, creating a strong vertical plume. By comparison, weak plumes are noticeably bent over by prevailing winds. Transport in the lower part of an eruption column, typically <2 km, is controlled by momentum, while buoyancy dominates above. If a sustained column rises to its neutral buoyancy level, it may spread out radially as a density-driven gravity current to form an umbrella cloud and disperse downwind (Figure 2a). Processes in the rising column are distinct from those in the spreading cloud and result in different deposit features beyond the plume corner (i.e. the point above which transport is dominated by horizontal spreading), resulting in deposits that show a marked break-in-slope in fall deposit thinning trends beyond this point.

In an alternative scenario, the eruptive jet initially fails to become fully buoyant (Figure 2b). Instead, the hot gas-particle mixture collapses downward, traveling along the ground as a pyroclastic density current (PDC). As the PDC propagates, it entrains ambient air into the front and top of the current, which heats and expands, reducing the density of the mixture until it becomes buoyant and rises. These ground-hugging currents can loft huge volumes of ash into the atmosphere, feeding a buoyant, vertical column known as a co-PDC plume (or co-ignimbrite plume if the flow is pumice-rich). Because initial updraft velocities near the ground are extremely low (only a few m/s), the rising thermals only entrain the finest particles[E1]. For this reason, co-PDC fall deposits consist primarily of fine ash <63 μm diameter. One well-documented example is the blast ashfall from the 18 May 1980 eruption of Mount St. Helens, Washington (USA), created by a co-PDC plume that rose 35 km above sea level (Case study box 1).

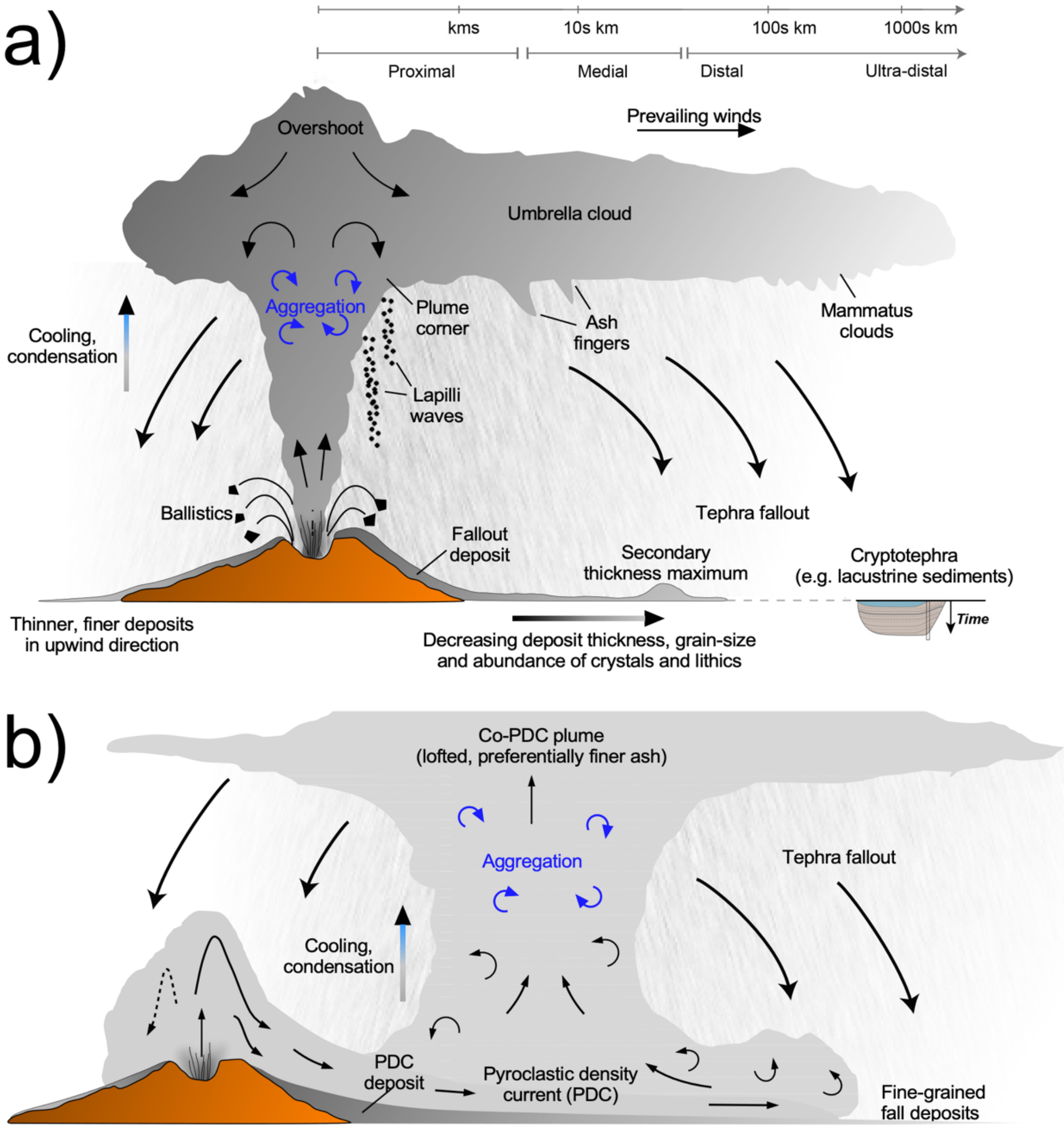

Figure 2. Processes governing tephra fallout from (a) a sustained, buoyant eruption column, and (b) an unstable column producing pyroclastic density currents (PDCs). Note the co-PDC plume of preferentially finer particles elutriated out of the current. Shifts between buoyant and collapsing plume dynamics may result in interbedded PDC deposits within a proximal fall sequence. However, finer grained layers of co-PDC ash can preserve well beyond the runout of PDCs. Blue arrows show regions of the plumes where the highest rates of particle aggregation are expected to occur due to cooling, moisture condensation, particle collision, and sticking.

The largest clasts ejected by volcanic eruptions are ballistic blocks and bombs, which range in size from 64 mm to several meters across. Proximal accumulation of bombs can eventually form welded fallout deposits (e.g., Askja 1875 in Iceland). Ballistics travel through the air without being significantly affected by the volcanic plume or wind field and their trajectories are mostly controlled by their shape and ejection angle. These clasts disperse close to the source area, generally within 4– 5 km from the crater. Some eruptions produce irregular areal distributions of ballistics whereas others show a pattern of decreasing block size with distance from the vent. Less frequently, larger clasts may deposit farther than smaller blocks due to complex interactions between block mass, shape, and drag.

Ballistic block transport can be modeled with a momentum balance equation:

$$\frac{d\vec{v}}{dt} = -\frac{\rho_a C_D A(\vec{v}-\vec{u})|\vec{v}-\vec{u}|}{2m} - \vec{g} \qquad (1)$$

where v is the block velocity, u is the ambient gas velocity (wind), ρ_a is the density of ambient air, A is the cross-sectional area normal to the ambient gas flow, C_D is the drag coefficient, m is the block mass and g is gravitational acceleration. Drag coefficient depends on Reynolds number, clast shape, and surface roughness, and that of ballistic blocks vary from 0.6–1.2 according to wind tunnel experiments.

In contrast, transport of smaller particles in the rising column is dominated by turbulent eddies. Particles that are small enough to be well coupled to the gas phase remain aloft if updraft velocities exceed the gravitational settling of individual clasts (Eq. 2). Mid-range-sized clasts, approximately >1 cm diameter, tend to decouple from the gas-particle mixture and may even shed directly from the column margins (see *lapilli waves* in Figure 2a). As deposition continues, the mass of particles within the plume decreases with height. For the remaining particles transported into the spreading cloud, sedimentation is controlled by several factors. Individual particle settling is governed by the terminal settling velocity (V_t):

$$V_t = \left(\left(\frac{4gD}{3C_D}\right)\left(\frac{\rho_p-\rho_a}{\rho_a}\right)\right)^{1/2} \qquad (2)$$

where D is the particle diameter, ρ_a is the atmosphere density, and ρ_p is the particle density. The drag coefficient C_D is controlled by the shape of the particle, the particle/fluid density ratio and the Reynolds number (*Re*), which describes the ratio of inertial to viscous forces:

$$Re = (\rho\, V_t\, D)/\mu \qquad (3)$$

where μ is the dynamic viscosity of the fluid and ρ its density. For particles with high *Re* (>500), flow around the falling particle is fully turbulent, and C_D is largely a function of particle shape. For intermediate *Re* ($20 < Re < 130$), the flow around the particle is transitional — a wake forms and grows downstream of the particle. Stokes flow, when no wake is present at the rear of a falling particle, occurs when $Re<0.1$ and, under this condition, C_D can be approximated by Stokes' Law.

As a volcanic plume disperses downwind, its airborne particles are efficiently sorted according to their settling velocity. The larger and denser particles fall more quickly and deposit closer to the vent, resulting in finer grained, thinner deposits with distance from source (Figure 2a). Fall deposits are typically elongated in the downwind direction due to prevailing winds. Windless cases are rare, but they do occur, producing deposits that are nearly circular about the vent. However, several other processes can influence tephra dispersal patterns, including *aggregation* and *gravitational instabilities*. At sufficient concentrations, fine particles collide and stick together, forming *ash aggregates*[6]. Dry conditions in the plume combined with electrostatic forces create loosely bound ash clusters – these aggregates have poor preservation potential in the geologic record. By comparison, humid, condensing conditions in volcanic plumes lead to more dense, compact pellets of ash, also known as accretionary lapilli. These tend to be more durable as secondary mineral growth from liquid films may increase their mechanical strength[7]. Moreover, such aggregates may survive impact with the ground and are more likely to be preserved in deposits. Depending on weather conditions at the time of eruption, frozen, ice-rich accretionary lapilli can form. However, they may be transient in the deposit record as they have been observed to melt after fallout and turn into slush. The density and size of ash aggregates control their residence time in the atmosphere. Fine ash (particles <63 μm) incorporated into accretionary lapilli fall out much sooner than they would have by single-particle settling. In contrast, coarse ash and lapilli might settle more slowly if they are incorporated into fluffy, loose aggregates due to increased drag (the so-called *rafting effect*[8]). The fundamental role of ash aggregation was recognized during the 18 May 1980 eruption of Mount St. Helens (USA), where *en masse* sedimentation of ash aggregates from the downwind cloud produced a locally thicker deposit, known as a secondary thickness maximum (Figure 3). This process was later observed in other cases such as the eruptions of Hudson volcano (Chile) in 1991 and the Mount Ruapehu (New Zealand) in 1996.

Other factors that can hasten the deposition of fine particles include formation of gravitational instabilities and capture of fine-grained particles in the wake of falling, coarser clasts. An example of an instability is an ash-laden downdraft that forms as particles collect at the base of a spreading cloud. These locally denser, descending regions may be observed as finger-like structures similar to virga in rain clouds (*ash fingers* or mammatus clouds; Figure 2).

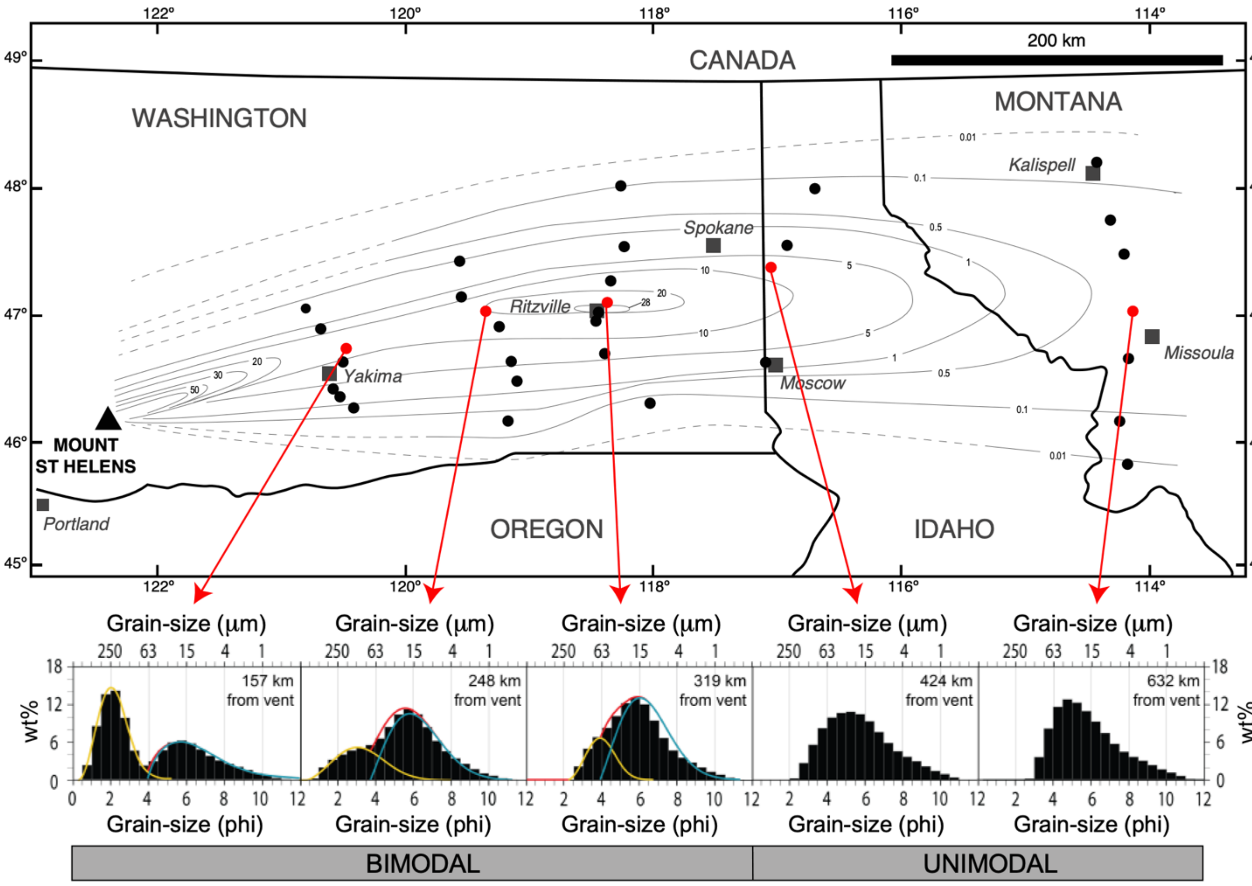

Figure 3. Isopach map of the 18 May 1980 Mount St. Helens (USA) tephra-fall deposit with associated grain-size distributions at different locations along the dispersal axis. The grain-size distribution transitions from

strongly bimodal within ~350 km from the volcano to unimodal beyond (modified from [F1]).

[INSERT in main text Case Study box 1 – "The Mount St. Helens (USA) eruption of May 18, 1980"]

Characterizing fall deposits and eruption source parameters

Studies of volcanic fall deposits are typically based on two pillars: 1) field-based stratigraphy and mapping of the deposit; and 2) laboratory-based analysis of physical characteristics, such as grain-size distribution, clast densities, textures, and proportions of different clast types (components) within the deposit. Field observations provide the fundamental basis for constraining the temporal and spatial evolution of an eruption. The best strategy for obtaining good coverage of a fall deposit considers the full picture of downwind, crosswind, and upwind features (Figure 2), integrating information from multiple outcrops and mapping the distal extent of the deposit. Deposit characteristics at variable stratigraphic heights (grading, juvenile/lithic content, type of contacts within a single tephra section sequence) can be complemented by other features (thickness data, maximum clast values), which in turn can be used for calculations of the main eruption source parameters (ESPs) such as erupted volume, mass eruption rate or plume height. All of these aspects assist eruption classification[9] and provide insights into eruptive processes.

Tephra dispersal, volume, and plume height

Measurements of deposit thickness (or mass per unit area) from across the tephra-fall deposit are used to establish dispersal extent and axis. These data can be used to produce isopach (or isomass) maps (Figures 3, 4) and to establish deposit thinning patterns, whose integration provides an estimate of mass or volume of the tephra-fall deposit which, combined with direct observations of eruption duration, may in turn be used to derive spatial variations in sedimentation rate. Several volume (or mass) calculation techniques are available in the literature[9-11], which show that distal fall volume can be significant in tephra-fall deposits. Diverse methods are routinely adopted to identify if deposits are incomplete due to erosion or deposition on water in case of eruptions from volcanoes near the coast. Although distal data are commonly difficult to obtain, rapid measurement campaigns on fresh tephra blankets have allowed detailed reconstruction of select, well-characterized deposits (Figures 3, 4). Similarly, ultra-proximal measures are generally difficult to collect due to rapid destruction (by subsequent activity) or challenging site access. Generally, isopach contours give a first idea of dispersal power and of wind conditions during the eruption. Elongated isopachs are typical, but there are exceptional cases of no-wind conditions reflected in nearly circular distributions.

Maximum clast-size data derived from tephra-fall deposits are used to derive maximum column height during an eruption. Maximum clast-size values represent the diameter of the largest clasts in a fall deposit at a specific location. In 2012, a wide community effort[12] resulted in specific protocols on maximum clast-size measurement techniques (i.e., three axes averaging techniques, extent of investigated area, number of clasts to be measured, lithics (ML) vs. pumice (MP)) to ensure comparability among different studies. Once MP or ML data are defined, these are used to compile isopleth maps (Figure 4) from which crosswind and downwind segments are derived (e.g. shape descriptors of the isopleth contours). Based on the shape of isopleth contours, numerical models[13] can be used to derive wind speed and maximum column height reached during an eruption because only a specific combination of plume height and wind allows a clast with certain characteristics (density and diameter) to reach a particular location.

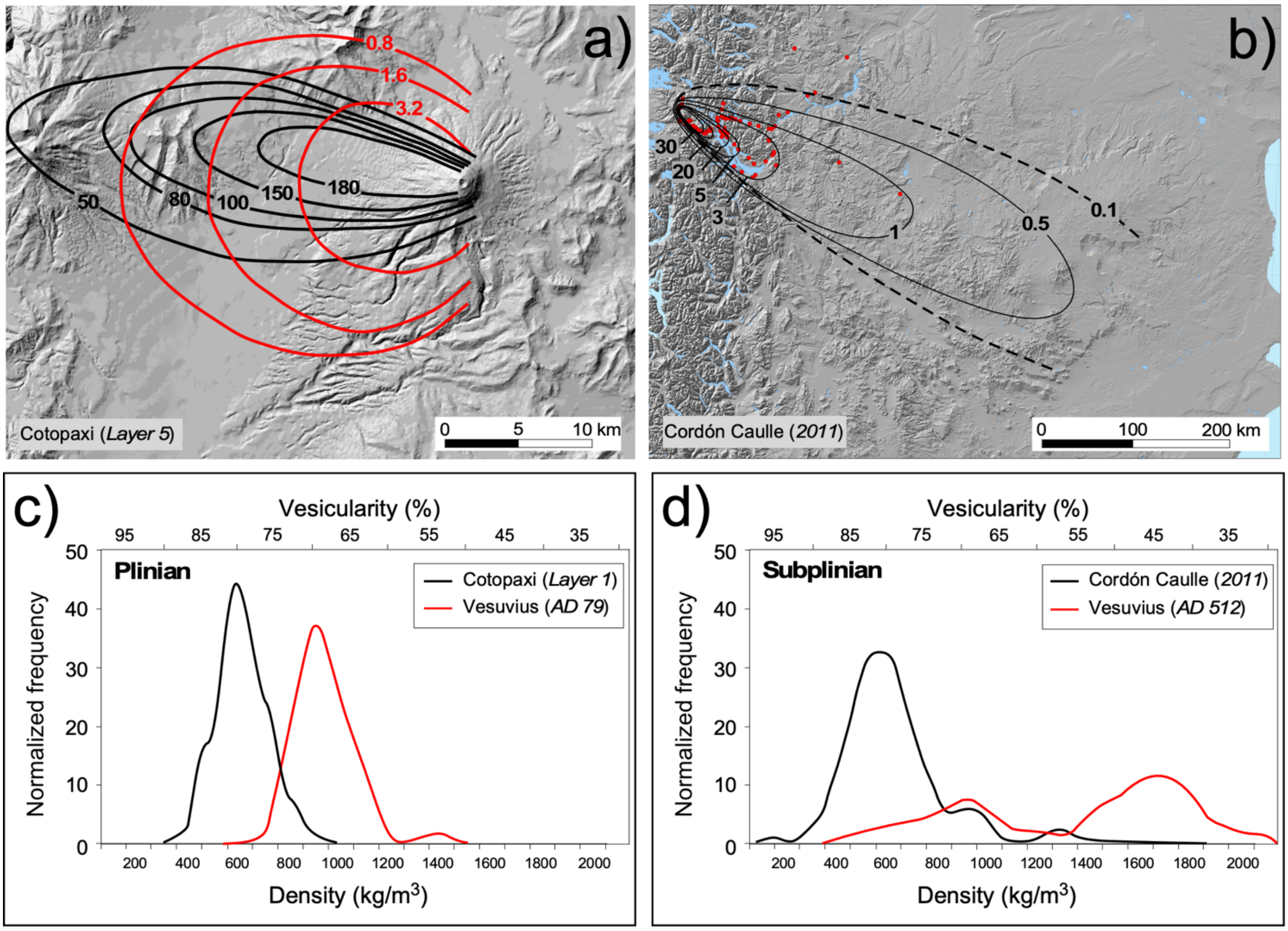

Figure 4. (a) Isopach (black lines; kg/m^2) and isopleth (red lines; cm) data for Layer 5 Plinian eruption at Cotopaxi volcano (Ecuador). (b) Isopach map of the Subplinian 2011 eruption at Puyehue-Cordón Caulle (Chile). (c) and (d) show the vesicularity/density distribution of juvenile clasts for Plinian (c - Cotopaxi volcano Layer 1 and Mount Vesuvius AD 79) and Subplinian (d - Puyehue-Cordón Caulle 2011 and Mount Vesuvius AD 512) eruptions; note the larger spread and bimodality of density for the Subplinian juvenile material compared to the Plinian events. Density data are from F2, F3 and F4.

[INSERT QR1 code Case Study box 2 – "The Puyehue-Cordón Caulle (Chile) eruption of 2011"]

Grain size, shape, and componentry

Once tephra samples are collected, sample grain size, componentry and clast shape information can be gathered to provide insight into eruption and deposition processes. The grain size of bulk samples may be determined by field sieving for size fractions >16 mm, which require large volumes of material, and by sieving in the laboratory for the remaining size fractions >63 μm. These measurements may be complemented by laser diffraction and optical methods or image analysis >~1 μm. Grain-size data are used to identify base-to top variations within an eruptive sequence at specific outcrops, track changing sedimentation processes with distance from the vent, and classify eruption style.

The grain-size distribution of tephra fallout deposits from 'dry' magmatic eruptions (not involving magma-water interaction) tends to be well sorted and unimodal. The median grain size decreases with distance according to the decreasing terminal fall velocities of clasts carried in the downwind cloud (Figure 5). When bimodal (or polymodal) distributions are observed (Figure 3), the co-location of multiple particle sizes may point to several different mechanisms. For example, ash aggregation provides a way to combine different particle sizes into larger clumps with similar fall speed. Alternatively, there may be multiple eruption processes represented by a single deposit, or clasts with very different densities (pumice, crystals, lithics) that result in the same terminal velocities. If clast densities are the explanation, the different modes would disappear if size classes were transformed into classes of terminal velocity.

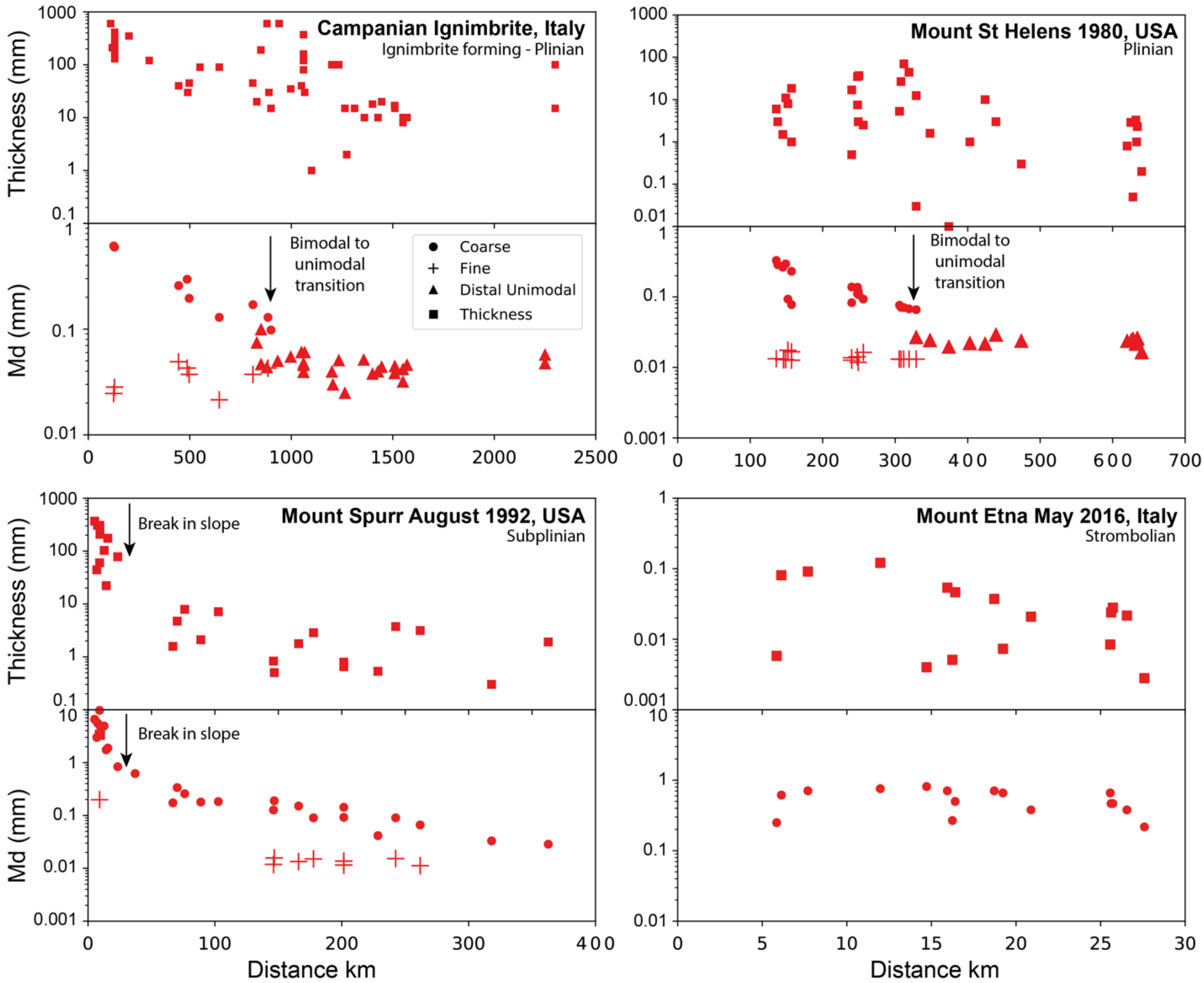

Figure 5. Trends in thickness and median grain size with distance from source for tephra fallout deposits from eruptions of different scale and type (modified from [F6]).

Grain-size data are also useful to derive statistical parameters (median, sorting) used to distinguish eruptive styles or emplacement dynamics (fall vs. ground-hugging flow). Integration of grain-size data from multiple outcrops by using different techniques (e.g., weighted average or tessellation strategies) can be used to derive the total grain-size distribution, that is, the granulometric distribution of the whole eruptive mixture ejected during an explosive eruption, a key input parameter for numerical simulation of cloud dispersal.

Sieving for grain size also prepares the material for componentry analysis. Each size class is separated by hand picking or point counting under a microscope to estimate the proportions of different components and their plausible origin. For example, particles interpreted as 'juvenile' (typically vesicular and glassy) are interpreted to represent fresh magma feeding the eruption. 'Non-juvenile' material may include lithic clasts from the breakup of pre-existing rocks. The juvenile clasts can be further distinguished by color, shape, vesicularity, and crystal content, which sheds light on the diversity of magma types, processes, and timescales involved in the eruption, as described below.

Pyroclast textural features

The main characteristics of pyroclastic material (density, vesicularity, morphology, grain-size distribution, shape) are controlled by magma properties (viscosity, volatile content, crystallinity) and ascent rates, which in turn influence the magma fragmentation dynamics (Figures 4, 6). Magma ascending quickly within the conduit will experience high decompression rates; when the characteristic time for cooling is shorter than the melt relaxation time, the resultant pyroclasts preserve the textural state of magma at fragmentation (porosity, crystallinity, bubble size and shape, clast morphology), resulting in its solid, highly vesicular counterpart. If time was available for relaxation (depending on eruption dynamics, eruptive temperature, fragmentation depth and clast size), bubble size, number and shape may change post fragmentation. Horizontal variations of temperature/viscosity and shear rate within the conduit can favor gas escape, with the formation of tubular pumices with deformed bubbles[4,14] and/or dense obsidian clasts[15]. Overall, pyroclasts generated by silicic, fast-ascending magmas have an exponential decrease in bubble number with increasing bubble size and exhibit low groundmass crystallinity, as typically shown by textural analysis of tephra associated with Plinian eruptions[14].

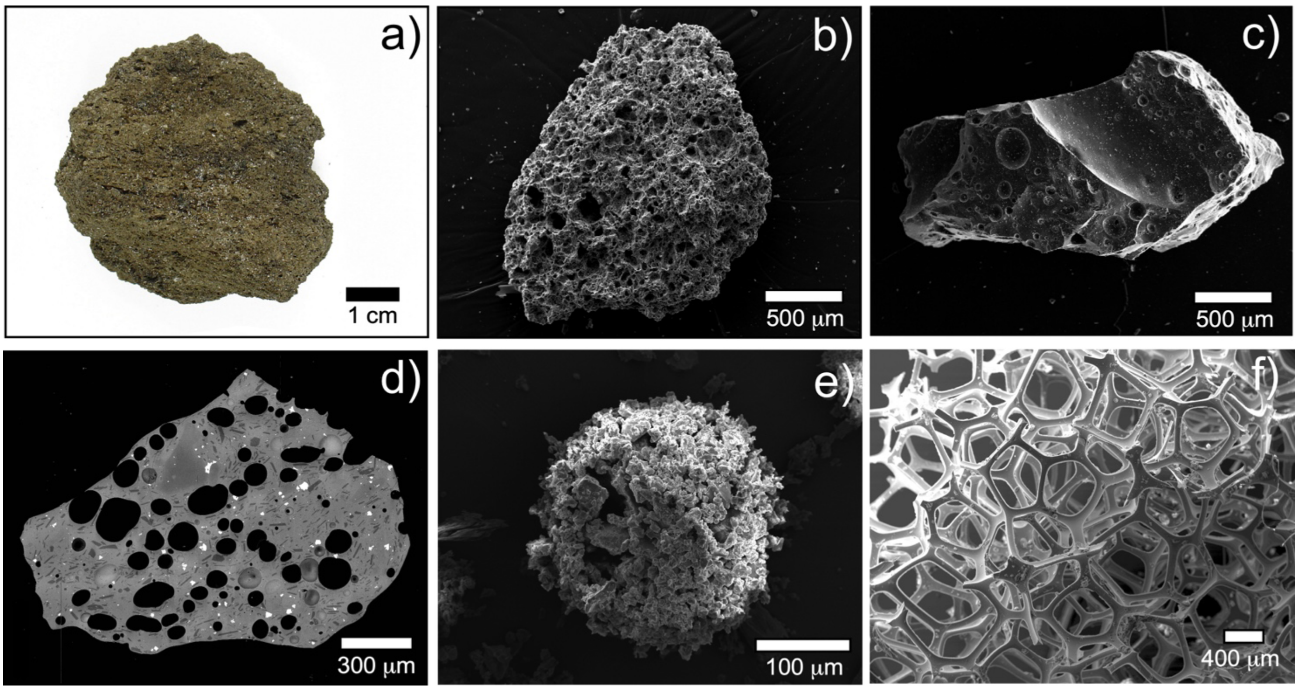

Figure 6. Diverse clast textures from tephra fall deposits. (a) Optical microscope image of a juvenile lapillus clast from a Plinian eruption of Cotopaxi volcano (Ecuador). (b-c) Three-dimensional scanning electron

microscopy (SEM) images of clasts from Eyjafjallajökull volcano, Iceland, in 2010 showing vesicular (b) and dense (c) textures. (d) Two-dimensional cross-section of a polished ash particle from the 2021 Tajogaite eruption, Canary Islands, showing vesicles (black) and crystals in the glass (medium gray). (e) Example of a loosely bound ash aggregate from the 2010 Eyjafjallajökull eruption. (f) Reticulite sample from Hawaii (courtesy of L. Folco).

With decreasing decompression rates and magma viscosity, bubble nucleation and growth will be facilitated by a combination of diffusion, decompression and coalescence, with the efficiency of the migration of the exsolved volatiles being counterbalanced by confining pressure, magma composition, crystal content and magma ascent velocity. Overall, growth of individual rising bubbles tends to dominate in low-viscosity magmas. Depending on magma ascent rates and initial gas contents, this process will eventually result in lower-efficiency fragmentation dynamics producing scoriaceous, coarse tephra blankets typical of basaltic volcanism (Hawaiian and Strombolian activity) accompanied by characteristic eruptive products such as Pele's hair or reticulite.

The size distribution of bubbles during magma fragmentation also plays a major role in the large variability of tephra morphology observed in nature, given the tight relationship between external shapes of pyroclasts and bubble microtexture. Externally sponge-like, or fluidal, up to dense clasts are evidence that brittle fragmentation is driven by bubble population (vesicle size and bubble walls) resulting in a large variety of morphologies and textures that can be measured and parametrized by several shape descriptors (e.g., concavity, sphericity, convexity). Some surface features, such as stepped and conchoidal fractures, indicate that brittle fragmentation has occurred and are commonly associated with phreatomagmatic deposits, where eruptions have occurred in the presence of magma/water interaction. Microlite content within the glassy groundmass also plays a major role in controlling magma rheology, and even small volumes of nanolite crystals can cause a substantial increase in melt viscosity, leading to explosive fragmentation.

Fall deposit classification

The wide ranges of eruptive styles and observational perspectives challenge a strict classification scheme. Early eruption classification used the morphology of the vent area (e.g. fissure vs. central vent, summit vs. flank). Later, locality-based names were ascribed to the activity seen at well- monitored volcanoes (Hawaiian, Strombolian, Vulcanian). These schemes required direct observations of eruptions and were largely qualitative, which made them difficult to apply to past events. Beginning in the 1970s, new classification schemes began to link eruption styles with their quantitative deposit features[16], using fall-deposit grain size as a proxy for fragmentation efficiency, and deposit dispersal as a proxy for eruptive intensity (Figure 7). This combination allowed volcanologists to distinguish the deposit characteristics of each eruptive style and link them to observable processes from modern eruptions. Still, some flexibility is required. Even in modern day, many eruptions are observed by volcano monitoring systems without an accessible or well-mapped deposit, meaning that the frameworks for classifying eruptions based on geophysical data and deposit features are continuously evolving. Here, we focus on how to classify eruption style using fall deposits as a means of connecting processes and products.

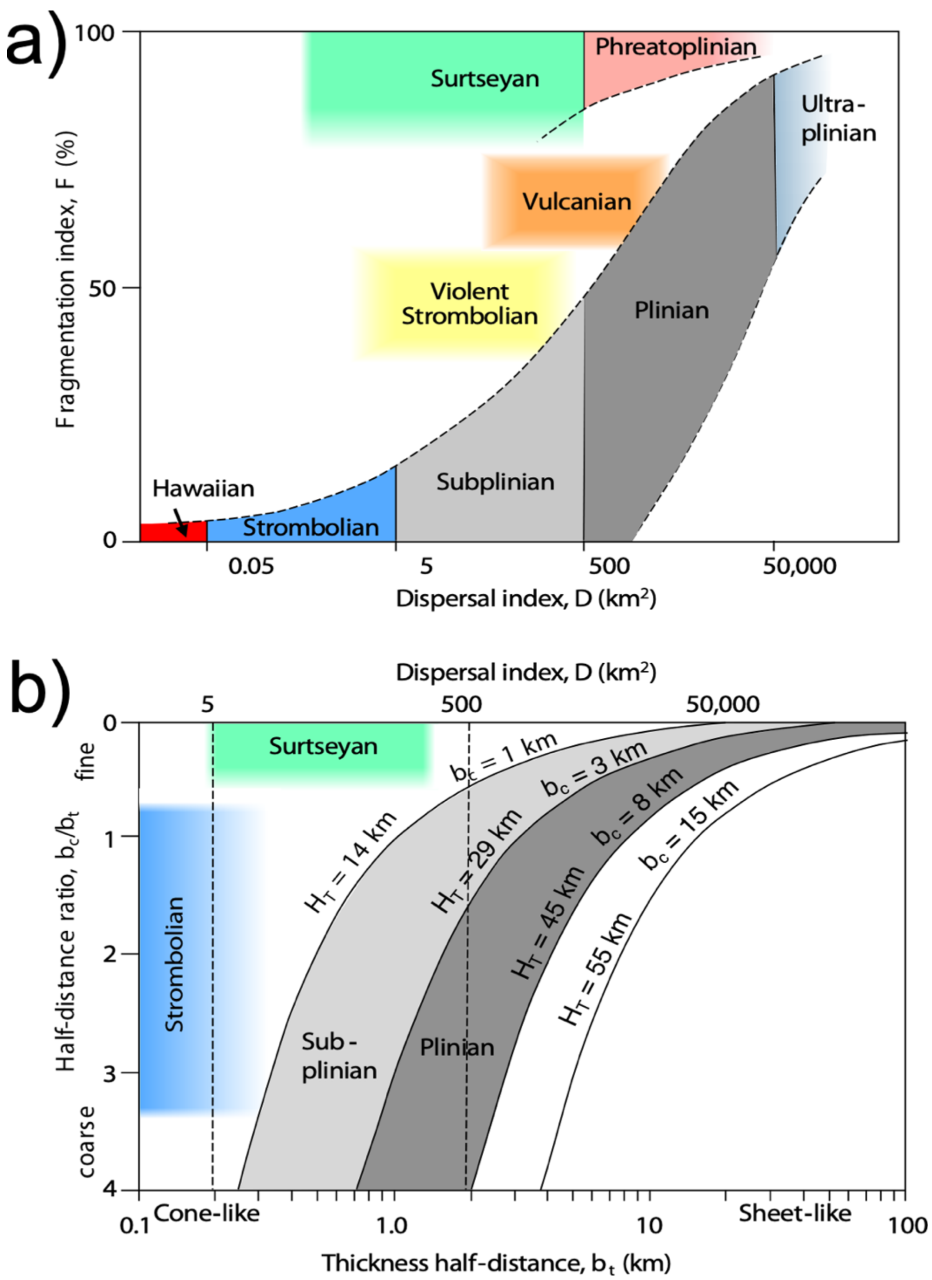

Figure 7. Classification schemes of eruptive styles based on tephra-fall deposit dispersal and grain size. (a) The Walker (1973) diagram plots dispersal index (D), which is the fall deposit area enclosed by the 0.01 Tmax isopach (where Tmax is the maximum thickness) against the fragmentation index (F), which is the percentage of material <1 mm at the point where the 0.1 Tmax isopach crosses the dispersal axis; modified from [9]. (b) The Pyle (1989) diagram is based on the thickness half-distance (b_t), which describes the thinning rate of the deposit, and clast half-distance b_c, which describes the fining of maximum clast size (H_T refers to maximum column height); modified from [16].

Hawaiian to Violent Strombolian

Low-intensity eruptions fed by mafic to intermediate magmas often result in pulsatory ejections of incandescent fragments and gas at variable heights, typically <5 km above the crater. Low vesicularity of tephra clasts and scarce lithics are the result of efficient outgassing, causing shallow, low-efficiency fragmentation and negligible conduit/crater erosion. Corresponding fall deposits are characterized by discrete to discontinuous tephra blankets of spatter and lapilli close to the source, rapidly thinning away, with variable vesicularity and crystal content (Figure 8). When the activity is characterized by sustained Hawaiian fountains, resulting layers of well-sorted lapilli have wider dispersal. In contrast, Strombolian, intermittent activity is characterized by emplacement of multiple spatter and ash layers or by showers of scattered fragments. In both cases, proximal accumulation of coarse-grained tephra often results in cone-building activity (tuff cones or scoria cones) and presence of variably welded products, often punctuated by partial failures and lava emissions[E1].

At higher intensity, the formation of scoria cones and more widespread tephra blankets characterize Violent Strombolian activity. With respect to the classical Strombolian regime, Violent Strombolian shows higher intensity, sustained dynamics and a highly pronounced unsteadiness (i.e., rapid fluctuations in mass eruption rate) resulting in the emplacement of hundreds of thin layers showing grain size and textural variability. The 1943 Parìcutin volcano (Mexico) and the 2021 Tajogaite volcano (Canary Islands) eruptions are classical examples of this type of eruption dynamic.

More rarely, basaltic Strombolian activity may result in even higher intensity, transient explosive events lasting a few minutes and leading to the formation of eruptive columns (e.g., Strombolian paroxysms at Stromboli volcano or fountaining at Mount Etna volcano, Italy). In these latter cases, tephra fall is characterized by greater dispersal under prevailing wind conditions, with proximal deposits showing high accumulation rates of tephra and ballistic ejection.

[INSERT QR2 code Case Study box 3 – "The Tajogaite (Canary Islands) eruption of 2021"]

Vulcanian

Vulcanian eruption style is commonly associated with the disruption of magma plugs or lava domes from magmas of intermediate to silicic composition. First described at Vulcano island (Southern Italy) during the 1888-90 eruption[17], the term has since grown to encompass a variety of eruptive styles. The main features are transient behavior with impulsive fragmentation of a rigid, partially degassed magma plug, lasting seconds to minutes. Each explosion forms a plume with buoyancy mostly related to thermal ascent, accompanied by ejection of cauliflower-textured to breadcrusted bombs and dense blocks along with fine ash. Occasionally, Vulcanian eruptions are accompanied by the formation of pyroclastic density currents.

Pressure build-up below the plug rebuilds continuously after each explosion, resulting in a repetitive dynamic which can last for months or years[E2]. For this reason, Vulcanian deposits tend to be stratified at very proximal sites, with each layer of ash or lapilli representing a single explosion (Figure 8). Long-lasting Vulcanian cycles may create hundreds of thin tephra layers. The ubiquitous presence of different types of large fragments (bombs or blocks) of juvenile material in the deposits of proximal ballistic showers or transported within pyroclastic density currents represents one of the most typical features of Vulcanian deposits. Juvenile particles are variably vesicular or dense, as a result of the disruption of different portions of the plug/dome. Prolonged eruption durations result in subcircular tephra-fall deposits distribution (circular isopach maps) reflecting low-level, variable wind conditions over time. The stratification of Vulcanian fall deposits makes it impractical to sample individual layers, and often a cumulative sample is representative of a specific period of activity.

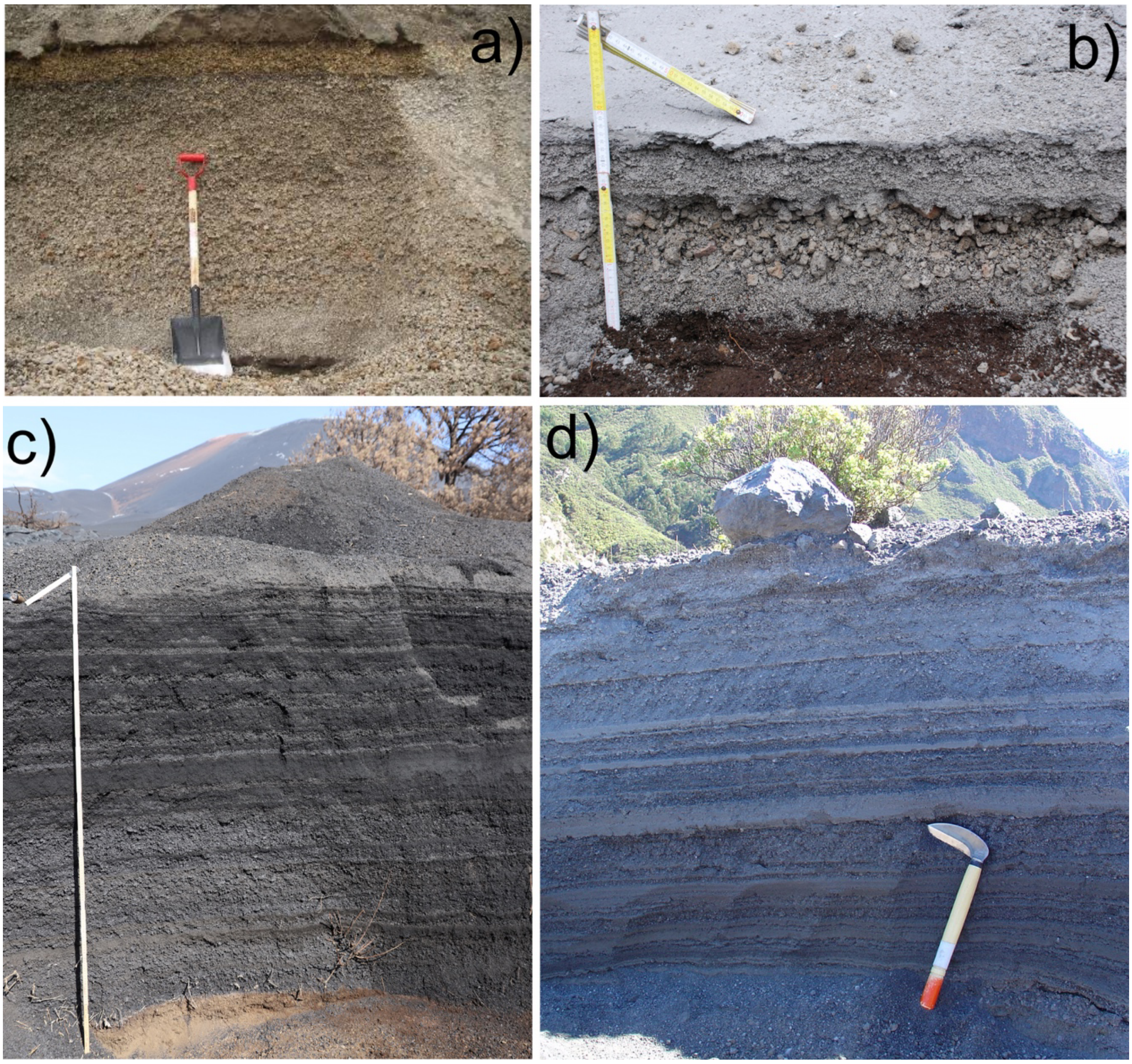

Figure 8. a) Proximal Plinian fallout deposit from Cotopaxi volcano (Ecuador). b) Medial Subplinian deposit from the 2011 eruption of Puyehue-Cordón Caulle (Chile). c) Proximal deposits from the 2021 Tajogaite (Canary Islands) Strombolian to Violent Strombolian eruption. d) The 1888-90 Vulcanian fallout deposit at Vulcano island (Italy). See also Case Study boxes 2, 3 and 4.

[INSERT QR3 code Case Study box 4 – "The Vulcano (Aeolian Islands, Italy) eruption of 1888-90"]

Plinian and Subplinian

Plinian eruptions represent some of the most powerful volcanic events on Earth. The defining characteristics are a high, sustained plume (20–35 km), efficient fragmentation, and fall-deposit dispersal across continental scales. Plinian deposits typically contain a dominant, homogeneous population of vesicular clasts, representing the product of deep ascent of a rapidly disintegrating magma foam. Due to their sustained dynamics, high intensity and evacuation of large volumes of magma, these eruptions can trigger caldera collapse and associated lithic breccias from pulverized country rock. Deposits in the near-vent area can preserve a multitude of complexities from the edge of the eruption column, including simultaneous fallout, localized PDCs, and ballistics.

At greater distances from source, the internal layers in Plinian fall deposits provide a more consistent record of the overall eruption tempo. This layering may be broadly categorized as simple, simple-stratified, and multiple. Simple Plinian deposits result from a steady eruption column that is sustained for several continuous hours. The deposits tend to be massive (non-stratified) or reversely graded, reflecting a progressive increase in mass eruption rate (Figure 8). Examples include deposits from the Santorini Minoan (Greece), Unit 5 Taupo (New Zealand), and 1902 Santa Maria (Guatemala) eruptions. Simple-stratified Plinian deposits contain internal bedding despite their origin from a single eruption with minimal time breaks. The beds represent shifts in eruptive intensity, fragmentation processes, or interlayering of PDC deposits within the fall sequence. The PDCs may originate from downdrafts (sloughing) off the margins of the column or transitions between buoyant and collapsing plume dynamics. Among the best examples of this type of deposits are the 18 May 1980 eruption of Mount St. Helens and the AD 79 eruption of Mount Vesuvius (Italy).

In contrast, multiple Plinian deposits result from notable time breaks within a single eruption spanning days to months. The temporary pauses are not long enough to allow significant erosion, reworking, and soil formation between successive fallout beds. But changing atmospheric conditions and subtle shifts in plume dynamics between the eruptive events create layers with distinct dispersal. Examples with multiple Plinian deposits include the 1815 Tambora volcano (Indonesia), 1982 El Chichón (Mexico), and 2008 Chaitén (Chile) volcano eruptions.

By comparison, Subplinian eruptions can also produce high plumes (up to ~20 km), but are characterized by column unsteadiness and less widely dispersed deposits. This behavior is associated with rapid changes in conduit dynamics, ejection velocity, or supply rate, resulting in short-lived pulses or eruption-column collapse. Tephra sedimentation is mainly controlled by low-level, weaker winds and, in the case of low vertical velocity of the plume, eruption columns may become bent over with no up-wind sedimentation. The corresponding pyroclastic deposits are produced by tephra fallout from oscillating, transitional to collapsing columns which can repeat in time over periods of days to weeks. Alternation of coarse tephra beds with finer layers form the complex architecture of Subplinian deposits, which are generally thinly stratified and finer grained at medial sites when compared to Plinian deposits. Partial collapses of the eruptive mixture may result in interbedding of PDC deposits within the fall sequence in proximal areas. At larger distances from the vent, or where PDCs are absent due to their strong directionality and topographic control, partial collapses of the eruptive column are only recorded by finer grained layers due to the temporary lowering of the eruption column.

Another significant distinction is that Subplinian deposits contain greater variability in pyroclast density, vesicularity, and texture (Figure 8). These features are explained by: (1) rapid decompression of volatile-rich magma pockets simultaneously with degassed magma that has stalled in the conduit, and (2) narrower conduits related to lower mass eruption rates, causing substantial boundary effects at the margins of the rising magma.

Surtseyan and Phreatoplinian deposits

The explosive interaction of magma and external water transforms the processes of tephra generation, transport, and deposition[E4]. Representing one end-member style of 'wet' volcanism, Surtseyan eruptions bring modest volumes of magma into contact with a water slurry (for example, during shallow submarine eruptions). This activity is characterized by explosive bursts ejecting jets of ash, mud, water, and steam. Individually ejected blocks leave trails of ash and steam along their ballistic trajectories, a feature known as cocks' tail jets[E5]. Examples of this type of volcanism are Surtsey volcano (Iceland) in 1963 (from which it takes the name), Capelinhos volcano (Azores) in 1957 and Mount Ruapehu (New Zealand) in 1971. Subaerial deposits from Surtseyan activity tend to be strongly stratified, poorly sorted and include a large amount of fine ash in proximal areas. "Vesiculated tuff" from accumulation of ash aggregates, or air bubbles trapped in wet ash, are a common feature of Surtseyan deposits, as well as the presence of scattered lithic clasts from the pre-eruption seafloor, quenched bombs incorporating wall rocks, and soft-sediment deformation structures.

In the case of large-scale, sustained explosive events, water involvement can shift a classic Plinian ('dry') eruption to a 'wet' Phreatoplinian eruption (examples are the 1875 Phase C of Askja volcano, Iceland, and the Oruanui eruption of Taupo volcano, New Zealand). Magmatic, dry Plinian eruptions are generally associated with well-sorted lapilli blankets that become progressively finer grained and less thick with distance from the vent. Lapilli-sized particles settle individually, allowing them to fractionate by size and density during atmospheric transport and wind selection. In contrast, hydrovolcanic activity forms poorly sorted, fine-grained deposits even close to the source. This key feature has two main explanations: (1) added moisture to the plumes leads to pervasive aggregation of ash, which rapidly scavenges fine-grained particles out of the atmosphere, and (2) 'wet' eruptions may produce additional fine ash due to magma-water fragmentation. In addition, large volumes of external water cool the eruptive mixture, favoring conditions for whole or partial column collapse.

During Phreatoplinian, Plinian, and Subplinian volcanism, it is possible for a significant portion of the tephra fall deposit to originate from co-PDC plumes that rise up from pyroclastic flows, as described in Figure 2. The fine-grained nature of particles in co-PDC plumes means that they can be transported over hundreds to thousands of kilometers from the source, contributing to their exceptionally wide dispersal.

Distal, ultra-distal, and cryptotephra deposits

During the largest explosive eruptions (VEI≥5), volcanic ash is transported by prevailing winds over hundreds (distal) to thousands (ultra-distal) of kilometers from the vent (Figure 2). Ash that eventually falls from the atmosphere may preserve as a tephra fall deposit layer in a range of depositional settings. Tephra-hosting sedimentary records often accumulate over thousands of years and include lacustrine (Figure 9a), marine (Figure 9c), peat, and cave sequences, as well as polar ice sheets and mountain glaciers.

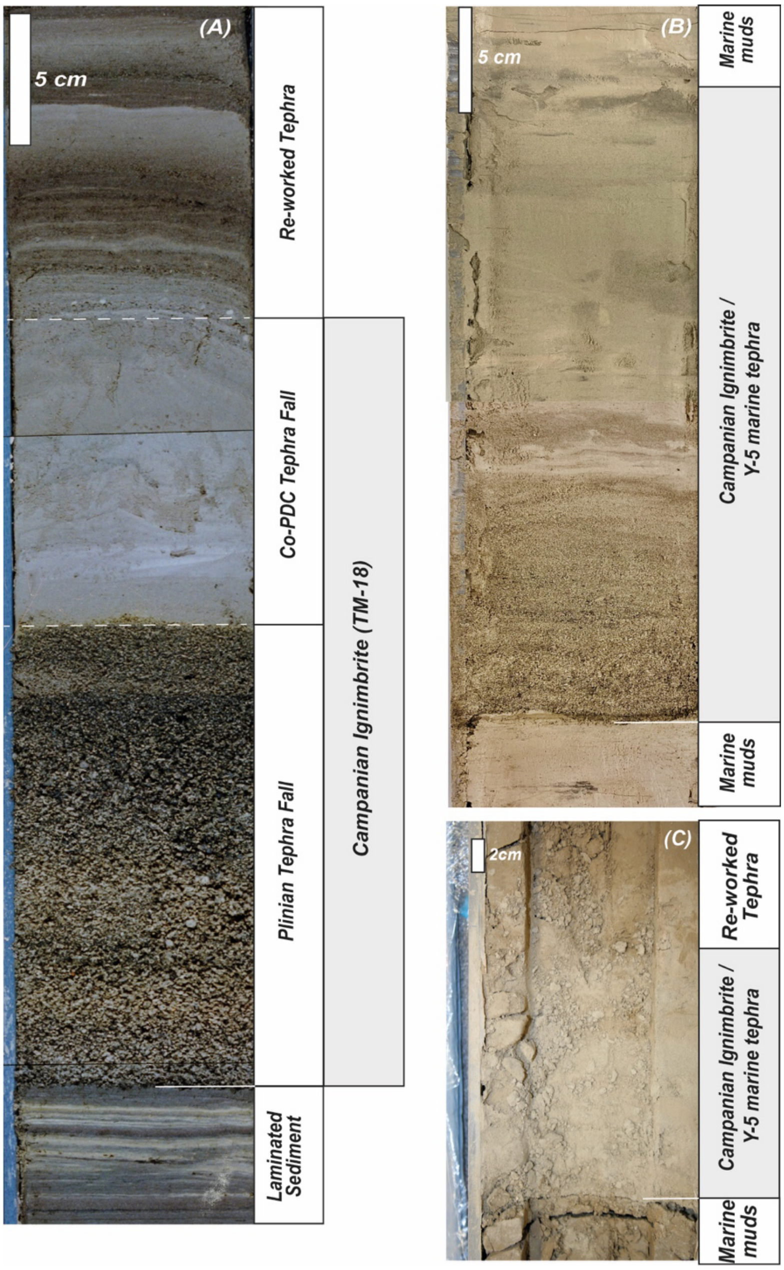

Figure 9. Distal tephra-fall deposits related to the 40-ka caldera-forming, Campanian Ignimbrite (CI) eruption of Campi Flegrei caldera, Italy, preserved in lacustrine and marine sedimentary records. (a) CI preserved in the annually laminated sediments of Lago Grande di Monticchio (core J10) 130 km east of Campi Flegrei (modified after [F5]). Note the Plinian fall deposit is separated from the overlying co-PDC ash by a sharp boundary. (b) CI preserved in the Tyrrhenian Sea core DED87-07, 200 km south-west of Campi Flegrei (image courtesy of S. Nomade). (c) Fine-grained CI preserved in the Aegean Sea core LC21, ~1225 km from source (after [F6]).

Owing to their widespread dispersal and near-instantaneous deposition, tephra-fall layers provide time markers that can be traced and correlated between disparate localities, using tephrostratigraphy, which offers a relative chronology. Where the source eruption is determined and dated, tephra layers provide absolute age markers, defining the field of tephrochronology[18]. In distal and ultra-distal settings, tephra-fall deposits are dominated by the lightest and most fine-grained components, the volcanic glass shards, while the denser or coarser clasts preferentially fall out closer to source (Figure 2). Eventually, with even greater distances from vent, the layer thins to the point of being invisible to the naked eye (i.e., cryptotephra).

Correlating tephra deposits between disparate localities and linking them back to proximal eruption deposits requires a detailed characterization of eruption units and their internal variability. Distally, the dominance of glass shards means that long-distance correlation relies on the chemical signature of the volcanic glass, which reflects the magma (melt) composition at the time of the eruption. Crucially, the glass composition of tephra does not differ greatly between proximal and distal settings. Chemical 'fingerprinting' of tephra deposits has traditionally relied on the major element composition of the volcanic glass, routinely determined using an electron microprobe (EMP) analysis. However, successive eruptions from the same volcanoes, or neighboring volcanoes, often share similar or overlapping major element chemical signatures. More recently, trace element characterization of the volcanic glass, typically achieved through laser ablation inductively coupled plasma mass spectrometry (LA-ICP-MS), has been used to resolve more diagnostic chemical fingerprints.

Cores extracted from distal sedimentary archives offer long, continuous records of tephra-fall layers (visible and cryptotephra), which are increasingly used to reconstruct eruptive histories, map prehistoric tephra dispersal, and generate more accurate eruption volume estimates. These sedimentary archives have the advantage of being sufficiently far from the erosive processes of active volcanic landscapes to add valuable detail to eruption records. In particular, they provide more accurate constraints on recurrence intervals of explosive eruptions over extended timescales, which plays an important role in assessing tephra-fall hazards.

Modeling tephra fallout

Tephra fall deposits can be reproduced using numerical models that simulate aspects of the tephra lifecycle[19], from fragmentation and plume dynamics to transport through the atmosphere, particle aggregation, and final deposition on the ground. These models provide insights into the dynamics of volcanic clouds and are key tools for developing long- and short-term hazard assessments[E3].

Three-dimensional (3D) models that calculate atmospheric tephra concentration and mass loading (or thickness) at the ground tend to employ Lagrangian or Eulerian frameworks. Lagrangian models track the positions of individual particles transported by the wind field and compute the values of interest (such as deposit load/thickness or atmospheric concentration) by averaging across cells in a predefined background grid. In contrast, Eulerian models solve the mass concentration equation of different particle sizes to calculate the values of interest at fixed spatial locations.

For most models used to simulate tephra fallout, the atmospheric conditions are supplied off-line as meteorological datasets (either reanalysis or forecast) from numerical weather prediction models. These datasets provide the main properties of the atmosphere (wind velocity, pressure, temperature, humidity and precipitation rate) on 3D grids and at a variety of time intervals. Spatial and temporal interpolations of the meteorological data are then required to align the atmospheric conditions with the setting of the transport model. In contrast, some models are based on a coupled approach between the numerical weather prediction model and the tephra transport model, meaning that the modeling of tephra transport is done together with that of the atmosphere, eliminating the need for spatial or temporal interpolations. Although the coupled approach enhances the simulation of tephra transport and sedimentation, the main drawback is higher computational cost compared to the traditional noncoupled approach.

Eruption source parameters are needed to define the initial conditions at the volcanic vent, including the start time, mass eruption rate, duration, total erupted mass, total grain-size distribution, physical properties of tephra particles, and vertical distribution of mass in the eruption column. These inputs are fundamental for obtaining accurate results. Mass eruption rate (amount of material released into the atmosphere per unit of time) is difficult to measure directly during eruptions and estimates usually derive from *a posteriori* analysis of deposits or observations collected during the eruption. The height of the eruption column is easier to measure and allows to constrain the mass eruption rate using semi-empirical relationships based on buoyant plume theory[20]. Modeled tephra particles are usually partitioned into a finite number of size and density classes based on the total grain-size distribution and componentry of erupted mixture (Figure 10a), with each class injected into the atmosphere according to vertical mass profiles that indicate the amount of material lost from the column per unit of time (Figure 10b). Source conditions may also be derived from eruption column models (both 1D integral models and 3D models)[E2] that offer the possibility of improving the representation of mass eruption rate and vertical mass profiles. Some models also include the ability to inject particles into the atmosphere by resuspension, i.e., the remobilization of tephra deposits by wind erosion[E9].

The processes simulated by both Eulerian and Lagrangian models, despite solving different equations, include advection, diffusion, and sedimentation of tephra particles, while neglecting inertial effects and particle-particle interactions. Advection moves particles according to the main components of the wind, while diffusion spreads particles horizontally and vertically to reduce concentration gradients. In the free atmosphere (i.e., above the boundary layer), tephra sedimentation is mainly due to gravity and is modeled by defining a terminal settling velocity. Wet deposition refers the process by which particles are scrubbed from the atmosphere due to ash aggregation and/or rainfall. This process is commonly modeled through the definition of scavenging coefficients that depend on the type of removal mechanism (in-cloud and below-cloud scavenging). Some models can also explicitly simulate particle aggregation. However, this process is computationally expensive, and it is more common to shift the total grain-size distribution coarser to account for the growth of aggregates.

Using tephra transport and sedimentation models, it is possible to produce maps that quantify the amount and spatial extent of tephra deposited on the ground or suspended in the atmosphere. For deposits, typical results include deposit thickness, ground load, and grain-size distribution. From these data, isopach and isopleth maps can be produced for model validation by comparing the numerical maps with those derived from field data (Figure 10c, d).

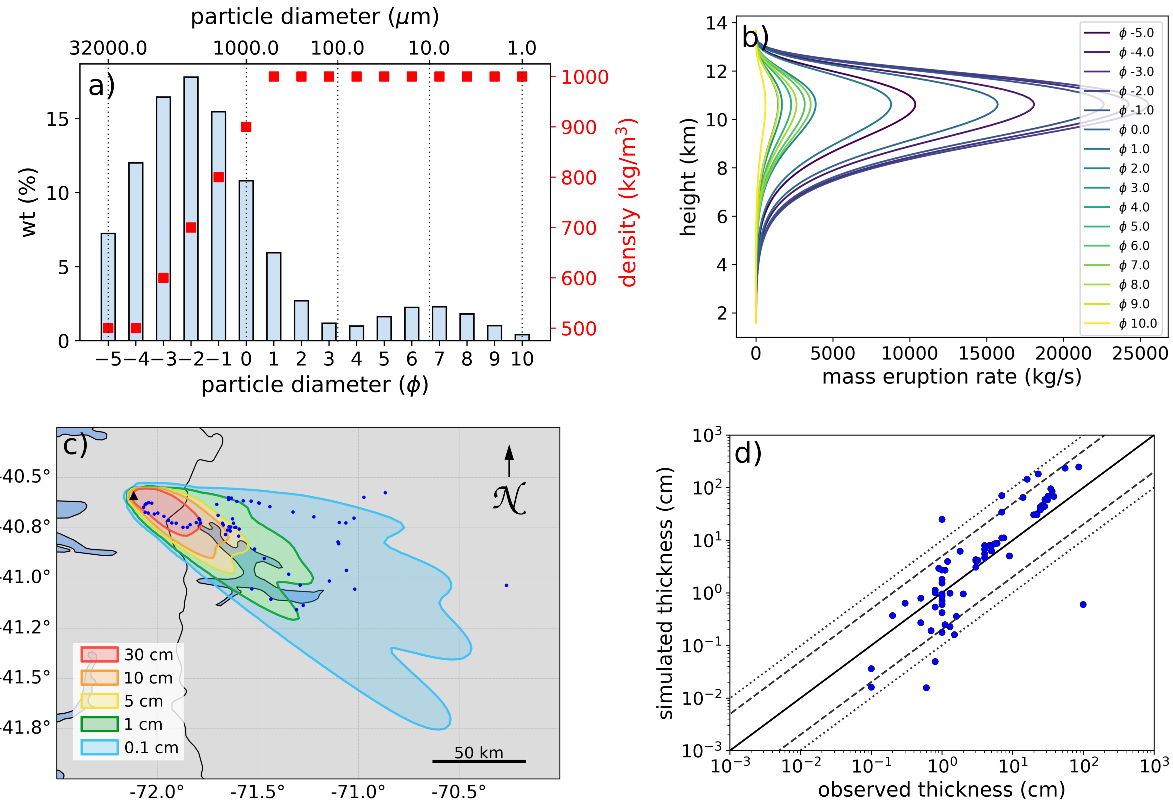

Figure 10. Deposit from the 2011 Puyehue-Cordón Caulle (Chile) eruption simulated using the FALL3D model [F7]. The deposit corresponds to the highest intensity phase of the eruption (Unit I, as described in [F8]). The simulated eruption duration is 30 h, starting at 18:45 UTC on 4 June 2011. Mass eruption rate is 4.16 x 10^6 kg/s, resulting in a total erupted mass of 4.5 x 10^{11} kg [F8]. (a) Total grain-size distribution and particle density extracted from [F8] and [F9]. (b) Vertical distribution profiles of mass of eruption rate for the 16 size classes forming the total grain-size distribution. (c) Deposit thickness simulated by FALL3D in cm. The blue dots indicate the sampling points as in [F7]. (d) Comparison of simulated versus observed deposit thickness. The solid line indicates a perfect match; dashed and dotted lines indicate deviations of five-fold and ten-fold, respectively.

The comparison between numerical and observational data also allows definition of inversion strategies aimed at numerically retrieving the ESPs from deposit observations (e.g., column height, mass eruption rate and total grain-size distribution). Solving the inverse problem involves running hundreds or thousands of simulations, each initialized with different sets of source parameters, to identify the best-fit terms that reproduce field observations. Over the years, different inversion algorithms have been applied and tested to address the main challenges in estimating these parameters from field data, such as the high number of parameters to estimate and the relatively small amount of observational data, especially for ancient eruptions.

Summary

Tephra generation is the result of a process of 'dry' or 'wet' fragmentation that occurs during magma ascent in the volcanic conduit, when high strain rates, velocities and overpressures force the liquid to respond brittlely to deformation. The combination of magma rheology, ascent velocity, volatile content and decompression rate gives rise to a wide range of eruption dynamics, which are linked to variable tephra products in terms of size, density and morphology. Thus, each eruptive style can be described by integrating tephra features with the characteristics of the associated deposits (e.g., texture, thickness, dispersal). Tephra studies are thus aimed at reconstructing the architecture of deposits in the field from which quantitative parameters can be derived for interpretation and classification of eruptive styles. Detailed study on tephra particles in the laboratory (grain size, texture, chemical composition) can help to further decipher eruption dynamics or correlate specific layers to distal or ultradistal environments. Tephra-fall deposits can also be used to refine numerical modeling of tephra dispersal in the atmosphere, which is essential for forecasting tephra behavior during eruption crises and informing long-term hazard assessments for communities living with volcanoes.

References

[1] S. Thorarinsson (1954). The eruptions of Hekla 1947–1948. II, 3. The tephra fall from Hekla. Vis Islendinga, Reykjavik, pp. 68

[2] M. Polacci, P., Papale, M. Rosi (2001). Textural heterogeneities in pumices from the climactic eruption of Mount Pinatubo, 15 June 1991, and implications for magma ascent dynamics. Bulletin of Volcanology, 63, 83-97.

[3] A. Pisello, U. Kueppers, K. Düffels, P. Nomikou, D.B Dingwell, D. Perugini (2023). The porosity of felsic pyroclasts: laboratory validation of field-based approaches. Bulletin of Volcanology, 85(11), 69.

[4] H.M. Gonnermann (2015). Magma fragmentation. Annual Review of Earth and Planetary Sciences, 43, 431-458.

[5] B. Zimanowski, R. Büttner, V. Lorenz (1997). Premixing of magma and water in MFCI experiments. Bulletin of Volcanology, 58, 491-495.

[6] R.J. Brown, C. Bonadonna, A.J. Durant (2012). A review of volcanic ash aggregation. Physics and Chemistry of the Earth, Parts A/B/C, 45–46, 65-78.

[7] S.B. Mueller, P.M. Ayris, F.B. Wadsworth, U. Küppers, A.S. Casas, P. Delmelle, J. Taddeucci, M. Jacob, D.B. Dingwell (2017). Ash aggregation enhanced by deposition and redistribution of salt on the surface of volcanic ash in eruption plumes. Scientific Reports 7, 45762.

[8] E. Rossi, G. Bagheri, F. Beckett, C. Bonadonna (2021). The fate of volcanic ash: premature or delayed sedimentation? Nature communications, 12(1), 1303.

[9] D.M. Pyle (1989). The thickness, volume and grainsize of tephra fall deposits. Bulletin of Volcanology, 51(1), 1–15.

[10] J. Fierstein, M. Nathenson (1992). Another look at the calculation of fallout tephra volumes. Bulletin of Volcanology, 54(2), 156–167.

[11] C. Bonadonna, A. Costa (2012). Estimating the volume of tephra deposits: A new simple strategy. Geology, 40(5), 415–418.

[12] C. Bonadonna, R. Cioni, M. Pistolesi, C. Connor, S. Scollo, L. Pioli, M. Rosi (2013). Determination of the largest clast sizes of tephra deposits for the characterization of explosive eruptions: a study of the IAVCEI commission on tephra hazard modelling. Bulletin of Volcanology, 75, 1-15.

[13] S. Carey, R.S.J. Sparks (1986). Quantitative models of the fallout and dispersal of tephra from volcanic eruption columns. Bulletin of Volcanology, 48, 109-125.

[14] C. Klug, K.V. Cashman, C. Bacon (2002). Structure and physical characteristics of pumice from the climactic eruption of Mount Mazama (Crater Lake), Oregon. Bulletin of Volcanology, 64, 486-501.

[15] J.E. Gardner, E.W. Llewellin, J.M. Watkins, K.S. Befus (2017). Formation of obsidian pyroclasts by sintering of ash particles in the volcanic conduit. Earth and Planetary Science Letters, 459, 252-263.

[16] G.P.L. Walker (1973). Explosive volcanic eruptions—a new classification scheme. Geologische Rundschau, 62, 431-446.

[17] G. Mercalli, O. Silvestri (1891). Le eruzioni dell'isola di Vulcano incominciate il 3 agosto 1888 e terminate il 22 marzo 1890: relazione scientifica della Commissione incaricata degli studi dal R. Governo. Stab. Bontempelli.

[18] D.J. Lowe (2011). Tephrochronology and its application: a review. Quaternary Geochronology, 6(2), 107-153.

[19] J. Paredes-Mariño, P. Forte, S. Alois, K.L. Chan, V. Cigala, S.B. Mueller, M. Poret, A. Spanu, I. Tomašek, P.Y. Tournigand, D. Perugini, U. Kueppers (2022). The lifecycle of volcanic ash: advances and ongoing challenges. Bulletin of Volcanology 84, 51.

[20] L.G. Mastin, M. Guffanti, R. Servranckx, P. Webley, S. Barsotti, K. Dean, C.F. Waythomas (2009). A multidisciplinary effort to assign realistic source parameters to models of volcanic ash- cloud transport and dispersion during eruptions. Journal of Volcanology and Geothermal Research, 186(1-2), 10-21.

References to other Chapters

[E1] Bonadonna et al., 2025, 4.4, Pyroclastic Density Currents, Charbonnier et al.

[E2] Bonadonna et al., 2025, 4.2, Tephra plumes (dynamics and modelling), Suzuki et al.

[E3] Bonadonna et al., 2025, 2.1, Eruptive Styles: Magmatic Eruptions, Cashman et al.

[E4] Sigurdsson et al., 2015, 27, Hawaiian and Strombolian Eruptions, Taddeucci et al.
[E5] Sigurdsson et al., 2015, 28, Vulcanian Eruptions, Clarke et al.
[E6] Sigurdsson et al., 2015, 29, Plinian and Subplinian Eruptions, Cioni et al.
[E7] Bonadonna et al., 2025, 2.2, Eruptive Styles: Hydrovolcanic eruptions, White et al.
[E8] Sigurdsson et al., 2015, 30, Phreatomagmatic and Related Eruption Styles, Houghton et al.
[E9] Bonadonna et al., 2025, 5.2, Aeolian Remobilization of Volcanic Ash, Dominguez et al.

Sources for Figures

[F1] J. Eychenne, S.L. Engwell (2023). The grainsize of volcanic fall deposits: spatial trends and physical controls. GSA Bulletin, 135(7-8), 1844-1858.

[F2] R. Cioni, A. Bertagnini, D. Andronico, P.D. Cole, F. Mundula (2011). The 512 AD eruption of Vesuvius: complex dynamics of a small scale Subplinian event. Bulletin of volcanology, 73, 789-810.

[F3] L. Gurioli, B.F. Houghton, K.V. Cashman, R. Cioni (2005). Complex changes in eruption dynamics during the 79 AD eruption of Vesuvius. Bulletin of Volcanology, 67, 144-159.

[F4] M. Pistolesi, A. Aravena, L. Costantini, C. Vigiani, R. Cioni, C. Bonadonna (2021). Explosive behavior of intermediate magmas: The example of Cotopaxi volcano (Ecuador). Geochemistry, Geophysics, Geosystems, 22(11).

[F5] K. Wutke, S. Wulf, E. Tomlinson, M. Hardiman, P. Dulski, J. Luterbacher, A. Brauer (2015). Geochemical properties and environmental impacts of seven Campanian tephra layers deposited between 40 and 38 ka BP in the varved lake sediments of Lago Grande di Monticchio, southern Italy. Quaternary Science Reviews, 118, 67-83.

[F6] S.L. Engwell, R.S.J. Sparks, S. Carey (2014). Physical characteristics of tephra layers in the deep-sea realm: the Campanian Ignimbrite eruption. London: The Geological Society of London.

[F7] A. Folch, L. Mingari, N. Gutierrez, M. Hanzich, G. Macedonio, A. Costa (2020). FALL3D-8.0: a computational model for atmospheric transport and deposition of particles, aerosols and radionuclides–Part 1: Model physics and numerics. Geoscientific Model Development, 13(3), 1431-1458.

[F8] M. Pistolesi, R. Cioni, C. Bonadonna, M. Elissondo, V. Baumann, A. Bertagnini, L. Chiari, R. Gonzales, M. Rosi, L. Francalanci (2015). Complex dynamics of small-moderate volcanic events: the example of the 2011 rhyolitic Cordón Caulle eruption, Chile. Bulletin of Volcanology, 77, 1-24.

[F9] C. Bonadonna, R. Cioni, M. Pistolesi, M. Elissondo, V. Baumann (2015). Sedimentation of long-lasting wind-affected volcanic plumes: the example of the 2011 rhyolitic Cordón Caulle eruption, Chile. Bulletin of Volcanology, 77, 1-19.

[F10] C.W. Criswell (1987). Chronology and pyroclastic stratigraphy of the May 18, 1980, eruption of Mount St. Helens, Washington. Journal of Geophysical Research—Solid Earth, 92(B10), 10237–10266.

[F11] C.W. Criswell (2021). A revised narrative of the May 18, 1980 Pinion eruption of Mount St. Helens: Changes in the conduit and magma supply. Journal of Volcanology and Geothermal Research, 419, 107388.

[F12] R.B. Waitt (2020). In the Path of Destruction: Eyewitness Chronicles of Mount St. Helens. Washington State University Press, 424 pp.

[INSERT QR code QR4 – "Further reading"]

Case Study box 1 (in the main text)

The Mount St. Helens (USA) eruption of May 18, 1980

The 1980 eruption of Mount St. Helens was a significant event in modern volcanology. Its wide range of eruption dynamics, combined with an extensive tephra deposit that fell entirely on land during daylight – in view of millions – provided a rare opportunity to link volcanic processes with their resulting deposits. The eruption on May 18, 1980, began with a landslide that unloaded a cryptodome growing inside the edifice. Rapid decompression triggered a laterally directed blast (Figure a), which developed into a fast-moving pyroclastic density current that devastated an area roughly the size of Chicago, USA (596 km^2). This current also lofted an enormous ash cloud (Figure b) – it rose 31 km above sea level and deposited a widespread layer of accretionary lapilli known as the blast ashfall. Simultaneously, the deeper magma reservoir at Mount St. Helens began to mobilize, ejecting vesicular pumice in a Plinian eruption that reached its peak plume height (19 km) four hours after eruption onset (Figure c). By mid-day, the eruption transitioned to partially collapsing behavior, sustaining a vent-derived plume simultaneously with ash-rich pyroclastic density currents (Figure d). Each phase of eruption can be identified in the tephra-fall record and timed using direct observations from eyewitness accounts (Figure e). The volume of fall deposits and pyroclastic density currents totaled ~2.3 km^3. This eruption marked a turning point in the integration of geologic fieldwork, real-time observation, and satellite remote sensing. The exceptional quality of data collected enabled researchers to develop new, quantitative models of volcanic plume injection and transport. It remains a benchmark case study for interpreting complex, multi-phase explosive eruptions and their tephra fall deposits.

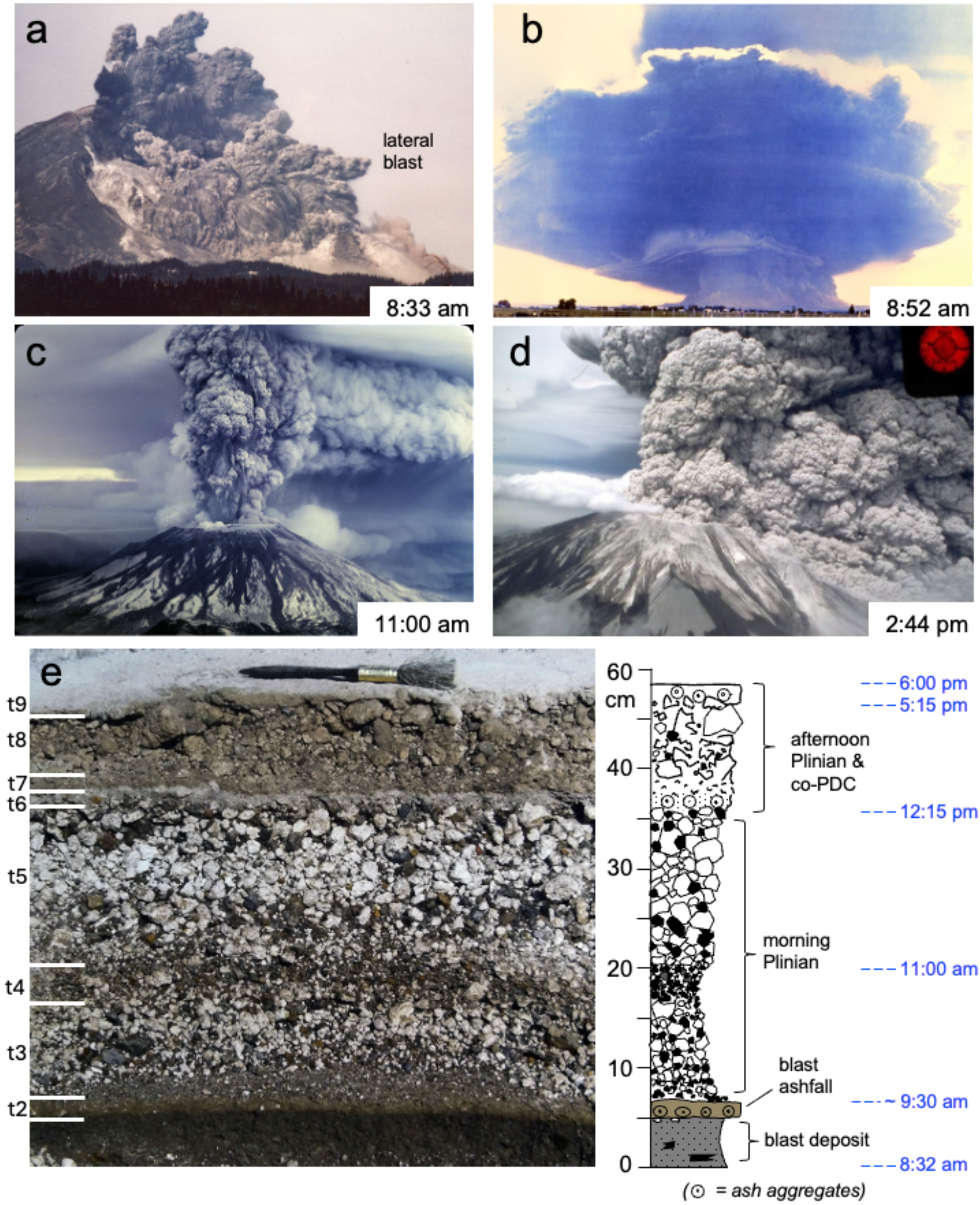

Volcanic processes and stratigraphy from the May 18, 1980, eruption of Mount St. Helens in Washington, USA. Images show: (a) the lateral blast, photographed by Gary Rosenquist; (b) the 31-km-high co-blast plume, photographed by Rocky Kolberg ~58 km northwest of Mount St. Helens; (c) mid-morning Plinian column, photographed by Richard G. Bowen, courtesy of the Bowen family; and (d) mid-afternoon activity showing both a vent-derived plume and ground-hugging currents, photographed by Joseph G. Rosenbaum. The stratigraphic record 4 km northeast of the vent (e), photographed by C. William Criswell, begins with a poorly sorted basal unit deposited by the lateral blast, containing abundant cryptodome clasts, altered lithics, and organic matter from shredded vegetation (base not shown in image). Directly above is a fine-grained, 1–3 cm thick layer rich in ash aggregates (the blast ashfall, t2), which is then overlain by pumice lapilli from the Plinian phase of the eruption (t3–t5). The Plinian layers are clast-supported and reversely graded (coarsening upward), which *records increasing eruption intensity through the morning. There is a sharp change in the tephra sequence after 12:15 pm, with distinctly more fine ash present (t6–t9). The afternoon layers contain ash-coated lapilli, representing clasts from the vent-derived plume that fell through the fine-grained ash lofted from ground-hugging currents as co-PDC plumes. Note brush for scale in (e). Times are in Pacific Daylight Time, indicating the onset of processes eventually forming the deposit based on [F10] [F11] and [F12].*

Case Study box 2 (with QR code QR1)

The Puyehue-Cordón Caulle (Chile) eruption of 2011

The 2011 eruption of Puyehue-Cordón Caulle (Chile) shows the typical characteristics of a long-lasting, Subplinian rhyolitic event. The eruption, following decades of repose of the volcanic complex and after a month of elevated seismic activity, started on 4 June 2011 and injected a large amount of tephra into the atmosphere. The initial, climactic phase lasted 24–30 h and produced 11–14-km-high plumes, with tephra rapidly reaching the Atlantic Ocean. The following phases were characterized by variable but overall lower intensity than the initial part, generating a complex tephra-fall deposit of ~1 km^3 with variable sedimentological features. The complexity of the deposits and the plume dynamics were also related to continuous wind shifts recognized during the entire eruption duration. Based on volume, plume height and mass flow rate, the eruption was classified as Subplinian, with the different phases characterized as VEI 3–5. Plume rise was strongly affected by wind during the entire eruption, with negligible upwind spreading and sedimentation. The tephra sequence in medial areas is characterized by alternating layers of lapilli representing the initial, highest intensity phase, coarse ash deposits, and ballistic bombs. Tephra-fall deposits are characterized by bimodal grain-size distributions, with both the mode and the fraction of the coarse subpopulation decreasing rapidly with distance from vent; the mode of the fine subpopulation is mostly stable. The total grain-size distribution of the climactic phase is also bimodal, with the coarse subpopulation representing 90 wt% of the emitted material. Tephra fallout affected a wide area of Argentina and Chile and impacted both the local and regional economy, including the evacuation of 4,000 people and agricultural economic losses of about ~$200 million USD. Air traffic was disrupted by temporary closure of several Patagonian airports and flight cancellations. After the impact caused by tephra fall during the eruption, the combination of dry climate of the Patagonian steppe, the strong wind and the fine grain size of the distal tephra-fall deposits caused severe issues related to ash resuspension in the years after the eruption.

The eruptive vertical plume and the mammatus of the cloud during the early phase of the 2011 eruption of Puyehue-Cordón Caulle. Co-PDC ash cloud is also visible on the left (Photo courtesy of C. Santana/AFP/Getty Images).

Case Study box 3 (with QR code QR2)

The Tajogaite (Canary Islands) eruption of 2021

The 2021 Tajogaite eruption of Cumbre Vieja (La Palma, Canary Islands) shows the characteristics of a hybrid event that was mostly effusive but also associated with widespread and impacting tephra fall deposits. The eruption occurred after 50 years of quiescence and was the largest eruptive event in the history of La Palma. It was preceded by relatively deep (10-25 km) and low-magnitude ($M_w<2$) seismic swarms starting in 2017, increased ground deformation, and detection of geochemical anomalies. The eruption started on 19 September 2021 with the opening of a new eruptive vent on the western flank of the Cumbre Vieja rift, and ended on 14 December, with a total duration of 86 days. The complexity of the eruption dynamics was related to a magma-gas decoupled system that resulted in the simultaneous emission of lava flows and tephra plumes from various vents. The tephra-fall deposit ($\sim 2\times10^7$ m^3) represents only 7%–16% of the total erupted volume (estimated at $\sim 17\times10^7$ m^3) as most of the erupted magma was emplaced as lava flows. Rapid gas segregation within the conduit and high magma ascent rate modulated the gas flux at multiple vents, giving rise to different explosive styles (ash-poor gas puffing, Strombolian, Violent Strombolian, and lava fountaining activity) and unsteady tephra accumulation. Tephra plumes varied in height during the eruption (1.5-8 km) as a consequence of variable wind conditions and mass flow rates. Tephra deposition was driven by different types of eruption dynamics and various size-selective sedimentation processes were observed, including particle aggregation and ash fingers, which have impacted the overall tephra dispersal. The resulting tephra-fall deposit was dispersed around the newly formed scoria cone without a clear preferential direction due to the complex and variable local wind pattern observed during the period spanned by this long-lasting eruption. Based on sedimentological features, the architecture of the tephra sequence was subdivided into three main units organized in layers and sublayers characterized by strongly stratified alternating sheets of lapilli and ash. These deposits correlate well at variable distances from the vent and can be associated with tremor data and lava effusion rates. Tephra and deposit features (grain size, dispersal, clasts vesicularity) fit well with those characteristics of Strombolian and Violent Strombolian eruptions discussed in the chapter.

The Tajogaite volcano activity during October 2021 as seen from the Est. The pyroclastic cone is already formed, and the activity is fed by multiple active vents characterized by variable eruptive styles.

Case Study box 4 (with QR code QR3)

The Vulcano (Aeolian Islands, Italy) eruption of 1888-90

The last eruption of the Island of Vulcano (Southern Italy), in 1888-90, represents the archetype of Vulcanian dynamics and it has been described as "[…] *not comparable to other styles of activities identified on volcanoes.* […] *It [did not reach] in any period the intensity of the Plinian stage, while it reached its majesty at the beginning and this together with the strength of his projections make it* *greater than the Strombolian type* [...]”[20]. The 1888-90 eruption started on 3 August 1888, when a roar and shaking of the ground was followed by the generation of a thick plume illuminated by lightning emerging from the main crater and launching of bombs across the northern sector of the island. Explosions with varying intervals persisted throughout the whole eruption until 22 March 1890 with few pauses, and were characterized by variable violence forming convective columns of 3-4 km. During major explosions, a dense and black plume quickly rose to kilometers in height, with bombs launched to several hundred meters from the crater. No lava dome or pyroclastic density currents were produced during the eruption. Two main “size” classes for the ejected tephra material were identified and defined as “blocks and bombs" that followed ballistic trajectories from the vent, and “sands and ashes” that deposited from the eruptive clouds as "rain". Non-juvenile products (blocks made of older lava and pale-grey ash) were also ejected, especially during the initial phase of the eruption. The main features of the tephra-fall deposits observable today are their overall fine grain size and limited dispersal due to a high number of low-intensity explosive events resulting in a repetitive sequence of stratified, parallel-bedded, thin layers of ash and lapilli with similar characteristics. The resulting tephra-fall sequence consisted of several meters of pyroclastic deposits around the vent rapidly thinning away from the cone, topped by a field of breadcrust bombs and blocks that covered the entire crater area. Componentry analyses show a large variability of juvenile material due to the presence of clasts with a wide density range resulting from the typical conduit dynamics of Vulcanian activity (i.e., fragmentation of degassed magma plugs) which often hinder separation among juvenile particles and “fresh” lithics.

The 1888-90 eruption crater seen from the southern rim of the La Fossa cone, with the ballistic bomb field in the foreground. The active fumarolic field is visible in the background.

ENCYCLOPEDIA OF VOLCANOES (3RD EDITION)

PART 3: Volcanic eruptions and associated products

Section 4: Explosive eruptions

Chapter 4.3 - Tephra fallout and associated deposits

– Additional Material –

Marco Pistolesi[1], Paul Albert[2], Alvaro Aravena[3], Samantha Engwell[4], Ulrich Kueppers[5], Federica Pardini[6], Kae Tsunematsu[7], Alexa R. Van Eaton[8]

[1]University of Pisa, Italy
[2]Swansea University, UK
[3]Universidad Católica del Maule, Chile
[4]British Geological Survey, UK
[5]Ludwig-Maximilians-Universität (LMU) Munich, Germany
[6]Istituto Nazionale di Geofisica e Vulcanologia, Italy
[7]Yamagata University, Japan
[8]U.S. Geological Survey, Cascades Volcano Observatory, Vancouver, Washington, USA

This is a peer-reviewed preprint submitted to *EarthArXiv*. The manuscript is part of Chapter 4.3 of forthcoming book: The Encyclopedia of Volcanoes, 3rd ed. Editors: C. Bonadonna, L. Caricchi, A. Clarke, P. Cole, J. Lindsay, J. Lowenstern, R. Robertson and M.L. Villegas, that will be published by Elsevier. As one of the first 20 chapters to be accepted for publication in the book, it is being allowed to be submitted to *EarthArXiv* as a preprint.

ENCYCLOPEDIA OF VOLCANOES (3RD EDITION)

PART 3: Volcanic eruptions and associated products

Section 4: Explosive eruptions

Chapter 4.3 - Tephra fallout and associated deposits

– Additional Material –

Marco Pistolesi[1], Paul Albert[2], Alvaro Aravena[3], Samantha Engwell[4], Ulrich Kueppers[5], Federica Pardini[6], Kae Tsunematsu[7], Alexa R. Van Eaton[8]

[1]University of Pisa, Italy
[2]Swansea University, UK
[3]Universidad Católica del Maule, Chile
[4]British Geological Survey, UK
[5]Ludwig-Maximilians-Universität (LMU) Munich, Germany
[6]Istituto Nazionale di Geofisica e Vulcanologia, Italy
[7]Yamagata University, Japan
[8]U.S. Geological Survey, Cascades Volcano Observatory, Vancouver, Washington, USA

Further reading

A. Aravena, R. Cioni, M. de' Michieli Vitturi, A. Neri (2018). Conduit stability effects on intensity and steadiness of explosive eruptions. Scientific reports, 8(1), 4125.

C. Bonadonna, M. Pistolesi, S. Biass, M. Voloschina, J. Romero, D. Coppola, A. Folch, L. D'Auria, A. Martin-Lorenzo, C. Pastore, M.P. Reyes-Hardy, F. Rodríguez (2022). Physical characterization of long-lasting hybrid eruptions: the 2021 Tajogaite eruption of Cumbre Vieja (La Palma, Canary Islands). Journal of Geophysical Research: Solid Earth, 127(11), e2022JB025302.

K.V. Cashman (2004). Volatile controls on magma ascent and eruption. Geophysical Monograph Series, 150, 109-124.

R. Cioni, M. Pistolesi, A. Bertagnini, C. Bonadonna, A. Hoskuldsson, B. Scateni (2014). Insights into the dynamics and evolution of the 2010 Eyjafjallajökull summit eruption (Iceland) provided by volcanic ash textures. Earth and Planetary Science Letters, 394, 111-123.

R. Constantinescu, J.T. White, C. Connor, P. Cole, K. Fontijn, J. Barclay, R. Robertson (2024). Estimation of eruption source parameters for the 2021 La Soufrière eruption (St Vincent): implications for quantification of eruption magnitude on volcanic islands. Geological Society, London, Special Publications, 539(1), 107-120.

C.W. Criswell (2021). A revised narrative of the May 18, 1980 Plinian eruption of Mount St. Helens: changes in the conduit and magma supply. Journal of Volcanology and Geothermal Research, 419, 107388.

S.M. Davies (2015). Cryptotephras: the revolution in correlation and precision dating. Journal of Quaternary Science, 30(2), 114-130.

F. Di Traglia, M. Pistolesi, C. Bonadonna, M. Rosi (2024). The last 1100 years of activity of La Fossa caldera, Vulcano Island (Italy): new insights into stratigraphy, chronology, and landscape evolution. Bulletin of Volcanology, 86(5), 47.

E.J. Liu, K.V. Cashman, A.C. Rust, S.R. Gislason (2015). The role of bubbles in generating fine ash during hydromagmatic eruptions. Geology, 43(3), 239-242.

A. Namiki, M. Manga (2008). Transition between fragmentation and permeable outgassing of low viscosity magmas. Journal of Volcanology and Geothermal Research, 169(1-2), 48-60.

M. Pistolesi, M. Rosi, R. Cioni, K.V., Cashman, A. Rossotti, E. Aguilera (2011). Physical volcanology of the post–twelfth-century activity at Cotopaxi volcano, Ecuador: behavior of an andesitic central volcano. GSA Bulletin, 123(5-6), 1193-1215.

M. Pistolesi, R. Cioni, C. Bonadonna, M. Elissondo, V. Baumann, A. Bertagnini, A., L. Chiari, R. Gonzales, M. Rosi, L. Francalanci (2015). Complex dynamics of small-moderate volcanic events: the example of the 2011 rhyolitic Cordón Caulle eruption, Chile. Bulletin of Volcanology, 77, 1-24.

A.C. Rust, M. Manga, K.V. Cashman (2003). Determining flow type, shear rate and shear stress in magmas from bubble shapes and orientations. Journal of Volcanology and Geothermal Research, 122(1-2), 111-132.

O. Spieler, B. Kennedy, U. Kueppers, D.B. Dingwell, B. Scheu, J. Taddeucci (2004). The fragmentation threshold of pyroclastic rocks. Earth and Planetary Science Letters 226, 139-148.

A. Tadini, F. Pardini, A. Bevilacqua, B. Bernard, P. Samaniego, M. de' Michieli Vitturi, A. Aravena, S. Hidalgo, O. Roche, N. Azzaoui, A. Neri, J. Aguilar (2025). Probabilistic tephra fallout hazard maps for Sangay volcano, Ecuador. Bulletin of Volcanology, 87(2), 1-23.

Sustainable Development Goals (SDGs)

Sources for Figures

[F1] J. Eychenne, S.L. Engwell (2023). The grainsize of volcanic fall deposits: spatial trends and physical controls. GSA Bulletin, 135(7-8), 1844-1858.

[F2] R. Cioni, A. Bertagnini, D. Andronico, P.D. Cole, F. Mundula (2011). The 512 AD eruption of Vesuvius: complex dynamics of a small scale Subplinian event. Bulletin of volcanology, 73, 789-810.

[F3] L. Gurioli, B.F. Houghton, K.V. Cashman, R. Cioni (2005). Complex changes in eruption dynamics during the 79 AD eruption of Vesuvius. Bulletin of Volcanology, 67, 144-159.

[F4] M. Pistolesi, A. Aravena, L. Costantini, C. Vigiani, R. Cioni, C. Bonadonna (2021). Explosive behavior of intermediate magmas: The example of Cotopaxi volcano (Ecuador). Geochemistry, Geophysics, Geosystems, 22(11).

[F5] K. Wutke, S. Wulf, E. Tomlinson, M. Hardiman, P. Dulski, J. Luterbacher, A. Brauer (2015). Geochemical properties and environmental impacts of seven Campanian tephra layers deposited between 40 and 38 ka BP in the varved lake sediments of Lago Grande di Monticchio, southern Italy. Quaternary Science Reviews, 118, 67-83.

[F6] S.L. Engwell, R.S.J. Sparks, S. Carey (2014). Physical characteristics of tephra layers in the deep-sea realm: the Campanian Ignimbrite eruption. London: The Geological Society of London.

[F7] A. Folch, L. Mingari, N. Gutierrez, M. Hanzich, G. Macedonio, A. Costa (2020). FALL3D-8.0: a computational model for atmospheric transport and deposition of particles, aerosols and radionuclides–Part 1: Model physics and numerics. Geoscientific Model Development, 13(3), 1431-1458.

[F8] M. Pistolesi, R. Cioni, C. Bonadonna, M. Elissondo, V. Baumann, A. Bertagnini, L. Chiari, R. Gonzales, M. Rosi, L. Francalanci (2015). Complex dynamics of small-moderate volcanic events: the example of the 2011 rhyolitic Cordón Caulle eruption, Chile. Bulletin of Volcanology, 77, 1-24.

[F9] C. Bonadonna, R. Cioni, M. Pistolesi, M. Elissondo, V. Baumann (2015). Sedimentation of long-lasting wind-affected volcanic plumes: the example of the 2011 rhyolitic Cordón Caulle eruption, Chile. Bulletin of Volcanology, 77, 1-19.

[F10] C.W. Criswell (1987). Chronology and pyroclastic stratigraphy of the May 18, 1980, eruption of Mount St. Helens, Washington. Journal of Geophysical Research—Solid Earth, 92(B10), 10237–10266.

[F11] C.W. Criswell (2021). A revised narrative of the May 18, 1980 Pinion eruption of Mount St. Helens: Changes in the conduit and magma supply. Journal of Volcanology and Geothermal Research, 419, 107388.

[F12] R.B. Waitt (2020). In the Path of Destruction: Eyewitness Chronicles of Mount St. Helens. Washington State University Press, 424 pp.